

This is a pre print version of the following article:

The bending of fully nonlinear beams. Theoretical, numerical and experimental analyses / Falope, Federico; Lanzoni, Luca; Tarantino, Angelo Marcello. - In: INTERNATIONAL JOURNAL OF ENGINEERING SCIENCE. - ISSN 0020-7225. - 145:(2019), pp. 1-37. [10.1016/j.ijengsci.2019.103167]

Terms of use:

The terms and conditions for the reuse of this version of the manuscript are specified in the publishing policy. For all terms of use and more information see the publisher's website.

19/12/2025 03:00

The bending of fully nonlinear beams. Theoretical, numerical and experimental analyses

Abstract

This paper deals with the equilibrium problem of fully nonlinear beams in bending by extending the model for the anticlastic flexion of solids recently proposed by L. Lanzoni and A.M. Tarantino [1] in the context of finite elasticity. In the first part of the paper it is shown, through a parametric analysis, that some geometrical parameters of the displacement field lose importance when slender beams are considered. Therefore, kinematics is reformulated and, subsequently, a fully nonlinear theory for the bending of slender beams is developed. In detail, no hypothesis of smallness is introduced for the deformation and displacement fields, the constitutive law is considered nonlinear and the equilibrium is imposed in the deformed configuration. Explicit formulas are obtained which describe the displacement fields of the inflexed beam, the stretches and the stresses for each point of the beam using both the Lagrangian and Eulerian descriptions. All these formulas are linearized by retrieving the classical formulae of the infinitesimal bending theory of beams. In the second part of the paper the theoretical results are compared with those provided by numerical and experimental analyses developed for the same equilibrium problem with the aim of justify the hypotheses underlying the theoretical model. The numerical model is based on the finite element method (FEM), whereas a test equipment prototype is designed and manufactured for the experimental analysis.

Keywords: Finite elasticity; Hyperelasticity; Equilibrium; Beam; Bending moment; Anticlastic curvature; Experimental pure-bending.

1. Introduction

2 The flexure of nonlinear beams has been widely investigated because of its
great relevance in many technical applications. Still today, however, a fully non-
4 linear analysis of this classic problem seems to escape to a convincing modelling.
This is basically due to the nonlinearities involved in the problem formulation,
6 such as those related to constitutive laws and to the impossibility of using the
smallness hypothesis for both the displacement field (which allows to impose the
8 equilibrium conditions in the undeformed configuration) and the displacement
gradient field (which permits to adopt linearized deformation measures). Even
10 when all nonlinearities are taken into account, as in the few cases developed in
the context of the finite elasticity, the complexity is such that only models that
12 describe approximately the behaviour of a body inflexed have been proposed in
Literature.

14 One of the first investigations in the framework of finite elasticity was carried
out by Seth [2], who studied a plate under flexure in the absence of body forces.
16 Based on the semi-inverse method, he assumed the deformed configuration of
the plate like a circular cylindrical shell, keeping valid the Bernoulli-Navier
18 hypothesis for cross sections. Moreover, he assumed that the stress depends
on the strain according to the linearized theory of elasticity. In his work, the
20 bending couples needed to induce the hypothesized configuration of the plate
together with the position of the unstretched fibre within the plate thickness
22 (neutral axis) were also assessed.

 The flexion problem of an elastic block was extended by Rivlin [3], using a
24 stored energy function for incompressible materials according to Mooney. The
deformation considered by Rivlin transforms the elastic block into a short cylin-
26 der with the base having the shape of a circular crown sector. No displacements
along the axis of the cylinder were taken into account, making the problem
28 as a matter of fact two-dimensional. Surface traction necessary to induce the
assumed displacement field was determined, showing that in the case of a Neo-
30 Hookean material, these surface tractions are equivalent to two equal and op-

posite couples acting at the end faces.

32 Other contributions, always based on Rivlin solution, were proposed by Er-
icksen [4], Carroll [5], Wang [6] and Aron and Wang [7]. Universal results in
34 finite elasticity for the bending of a rectangular parallelepiped into a cylindrical
annular sector are listed in review paper by Saccomandi [8].

36 Shield [9] studied the problem of the bending of a beam by assuming small
strains but large displacements. He retrieved the linear Lamb solution [10] for
38 the deflection of the middle surface of the beam. As remarked in this work, for
large values of the width-to-thickness ratio, the deflection profile is flat in the
40 central portion of the cross section and oscillatory near the edges.

All the aforementioned works address the bending problem in a two-dimensional
42 context, systematically neglecting the pure deformation of the cross sections. In
this way, the modelling of the problem was substantially simplified, since the
44 displacement field is assumed to be plane.

A wide amount of studies dealing the flexion with large deflections of beams,
46 under several loading and clamping conditions, can be found in the Literature.
A significant part of these studies was based on the solution of the Elastica
48 according to the well-known Euler-Bernoulli law for bending (*cf.* Love [11]).
After some studies about a cantilever beam subjected at its free edge to a con-
50 centrated vertical load, Wang et al. [12] proposed a straightforward numerical
approach to solve the equilibrium problem of beams under different load distri-
52 butions. On the same subject, other contributions were provided by Wang [13]
and Holden [14]. A comprehensive review on applications of the Elastica can be
54 found in the book by Frisch-Fay [15]. In all these works, a linear law between
the curvature and the bending moment was assumed.

56 Likewise to the Elastica, Reissner [16] modelled a beam as an inextensible
one-dimensional system considering in addition the shearing deformation. Using
58 the principle of virtual works, he derived a nonlinear equilibrium equation for
beams and subsequently extended the analysis to thin curved beams [17, 18].

60 In the framework of finite elements method (FEM) for nonlinear analysis of
structures, many works concerning the large displacements and large rotations

62 of beams were carried out. As an example, Bathe and Bolourchi [19] reported
both a total Lagrangian formulation and an updated Lagrangian formulation to
64 perform FEM analyses suitable for 3D beams. Both formulations were based
on incremental equilibrium equations and proper decomposition of stresses and
66 strains. Cubic interpolating functions were assumed to describe the displace-
ment field related to bending. This study shown that the updated Lagrangian
68 formulation is computationally effective, as confirmed by a number of sample
solutions about shallow arches and cantilever beams, including the case of an
70 initially curved beam. Although both displacements and rotations were consid-
ered large in this reference, the strains were assumed to be small.

72 A straightforward parametrization of the equation of motion suitable for
FEM formulation of beams was proposed by Simo [20]. In that work, the con-
74 figuration of a beam was completely described by an orthogonal matrix, from
which both the rigid rotations of cross sections and the position of the centroids
76 can be inferred. In addition, it was shown that the formulation reported by
Reissner [16] is exactly retrieved when a plane problem is considered.

78 In the works by Cardona and Geradin [21] and by Simo and Vu-Quoc [22],
a vector description of rotations was assumed and the parametrization of finite
80 rotations was discussed in detail. The governing equations were derived by
assuming that cross sections do not change and preserve their planarity during
82 the deformation process. The motion equations of beams were made explicit
both in spatial and material settings. For both static and dynamic situations
84 a FEM analysis was performed. Following this approach other contributions
are given in [23]. However, in these works, neglecting the quadratic part of the
86 Green–Lagrange strain tensor, small strains were considered and in addition a
linear constitutive relation was adopted.

88 Moreover, in all these works concerning beams under finite displacements
[19, 23] (as well as in the case of the Elastica [11]–[18] or in the case of models
90 developed in the context of the finite elasticity [2]–[9]), the pure deformation
of cross sections was completely neglected, because during deformation these
92 maintain their shape and size, changing rigidly just the position. On the con-

trary, according to a more adherent view to physical behaviour of beams, the
94 pure deformation of cross sections should always be taken into consideration,
since the longitudinal inflexion is always coupled to the transversal one. More
96 specifically, also cross sections are inflexed with a curvature which is opposite
to that longitudinal, and the two curvatures have comparable magnitudes. The
98 transversal deformation just described is known in Literature as anticlastic ef-
fect.

100 In this regard, it should be kept in mind that the pure deformation of the
cross sections is usually taken into account even in the classic linear bending
102 theory of beams.

Recently Lanzoni and Tarantino [1] proposed a fully nonlinear analysis of
104 solids under anticlastic bending. In [1], a three-dimensional kinematic model,
where the longitudinal bending is accompanied by the transversal deformation
106 of cross sections, is formulated. By following a semi-inverse approach, the dis-
placement field, containing some free unknown parameters, is obtained. Succes-
108 sively, through the equilibrium equations and the boundary conditions, these
free parameters are determined. The current paper continues this study, ad-
110 dressing specifically and developing further the analysis for beams, namely for
the particular case of solids with a predominant dimension on the other two.

112 Section 2 investigates the theoretical model. In particular, in Section 2.1, the
displacement field obtained in [1] and the constitutive law adopted are recalled.
114 In Section 2.2, the equilibrium equations in dimensionless form are derived. By
varying the geometrical and constitutive parameters, it was shown by means of
116 a numerical analysis that these equilibrium equations are substantially satisfied
at each point of the beam. Furthermore, this preliminary study shows that, as
118 the beam becomes more and more slender, some geometrical quantities of the
displacement field lose their physical meaning. Based on these observations,
120 the kinematics is reformulated in Section 2.3 and a fully nonlinear theory is
developed for the class of slender beams. Explicit formulas for stretches, Piola-
122 Kirchhoff and Cauchy stresses are provided. The nonlinear bending theory is
linearized in Section 2.4, by introducing the hypothesis of smallness for both

124 the deformation and displacement fields and getting the well-known formulas
of the linear bending theory of slender beams. The results provided by the
126 theoretical model are then compared in Section 3 with the results obtained by
the numerical and experimental analyses. In Section 3.1, the numerical model
128 developed for the bending of nonlinear beams, using the finite element method
(FEM), is presented and discussed in detail. The experimental apparatus spe-
130 cially designed and constructed for the large bending of beams is described in
Section 3.2. The experimental results are provided in terms of DIC monitoring,
132 i.e. the full-field optical monitoring technique. Displacement fields evaluated
with the theoretical model, the FE model and the experimental tests are com-
134 pared to each other in Section 3.3. Furthermore, particular attention is paid to
the evaluation of the anticlastic radius and to its variability inside of the cross
136 section as well as to estimate the reliability of the hypothesis of conservation of
planarity of the cross sections. Finally, conclusions are drawn in Section 4.

138 2. The theoretical model

2.1. Displacement field

140 In this Section, some authors' results for the finite anticlastic bending of
solids [1] are recalled and at the same time the notation is introduced.

142 Let us consider a hyperelastic beam $\bar{\mathcal{B}}$ composed of a homogeneous, isotropic
and compressible material, having the shape of a rectangular parallelepiped.
144 The width, height and length of this parallelepiped are denoted by B , H and L ,
respectively. Reference is made to a Cartesian coordinate system $\{O, X, Y, Z\}$
146 having the origin O placed in the centroid of the beam, as shown in Figure 1.
Although the formulation will be developed for a beam with a rectangular cross
148 section, it can be readily extended to beams with a generic cross section provided
that the symmetry with respect to the Y axis is maintained.

150 The undeformed configuration $\bar{\mathcal{B}}$ of the beam is assumed as the reference
configuration, whereas the deformed configuration is given by the *deformation*

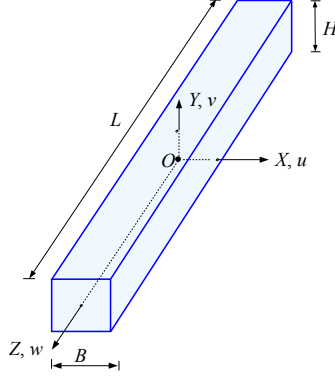


Figure 1: Prismatic beam $\bar{\mathcal{B}}$.

152 $\mathbf{f}: \bar{\mathcal{B}} \rightarrow \mathcal{V}$,¹ that is a smooth enough, injective and orientation-preserving (in the
 sense that $\det \mathbf{D}\mathbf{f} > 0$) vector field. The deformation of a generic material point
 154 P can be expressed by the well-known relationship

$$\mathbf{f}(P) = \mathbf{s}(P) + \mathbf{id}(P), \quad (1)$$

where $\mathbf{id}(P)$ and

$$\mathbf{s}(P) = u(P)\mathbf{i} + v(P)\mathbf{j} + w(P)\mathbf{k}, \quad (2)$$

156 are the position and displacement vectors of the point P . Into (2), the functions
 $u(P)$, $v(P)$ and $w(P)$ are the scalar components of $\mathbf{s}(P)$, whereas \mathbf{i}, \mathbf{j} and \mathbf{k}
 158 denote the unit vectors. The application of the material gradient operator $\mathbf{D}(\cdot)$
 to (1) gives

$$\mathbf{F} = \mathbf{H} + \mathbf{I}, \quad (3)$$

160 where $\mathbf{F}: \bar{\mathcal{B}} \rightarrow \text{Lin}^+$ and $\mathbf{H}: \bar{\mathcal{B}} \rightarrow \text{Lin}$ are the deformation and displacement
 gradients, respectively.² \mathbf{I} is the identity tensor. Points belonging to the de-
 162 formed configuration are indicated with an apex, $(\cdot)'$, and components u , v and
 w are referred to the reference system $\{O, X, Y, Z\}$. Fixed notation, we now
 164 move to the description of the displacement field.

¹ \mathcal{V} is the vector space associated with the three-dimensional Euclidean space \mathcal{E} .

² Lin is the set of all (second order) tensors whereas Lin^+ is the subset of tensors with positive determinant.

In order to determine the displacement field of a nonlinear beam longitudinally inflexed, the following basic hypotheses are introduced.

1. The beam is inflexed longitudinally with constant curvature. Namely, each rectilinear segment of the beam, parallel to the Z axis, is transformed into an arc of circumference.
2. Plane cross sections, orthogonal to the Z axis, remain as such after the beam has been inflexed. Cross sections can deform only in their own plane and all in the same way.
3. As a result of longitudinal inflexion, the beam is inflexed also transversally. Even this transversal inflexion has constant curvature, in such a way that any horizontal plane of the beam is transformed in a toroidal open surface.
4. Slender beams with compact cross sections are considered.

The longitudinal inflexion can be considered as generated by the application of a pair of self-balanced bending moments or by a geometric boundary condition which imposes a prescribed relative rotation between the two end faces of the beam. For both situations, the first assumption, indispensable in a nonlinear context, requires a uniform inflexion of the beam. The second hypothesis is known as Bernoulli-Navier hypothesis, and it is very popular in the linear mechanics of slender beams under pure bending. This assumption, which predicts the conservation of the planarity of cross sections, provides sufficiently accurate results in the above linear theory, while in our context it is certainly less reliable. In any case, it is expected that such an assumption appears better verified for the central portion of the cross section and less for points close to the boundary, where displacement components out of the plane are predictable. The third hypothesis is clearly approximated, since the transversal curvature in general will not be constant, but it will depend on the position of the material point considered within the cross section. However, these first three hypotheses will be better satisfied in the case of compact cross sections, in which height and width are comparable and when the length of the beam is greater than height and width. Namely, in the geometrical conditions specified by the fourth

hypothesis.

196 In their analysis, Lanzoni and Tarantino [1], considering only the first three
hypotheses, deduced the following expressions for the components of the dis-
198 placement field:

$$\begin{cases} u = -X + r e^{-\frac{1}{r}(Y+OA)} \sin \frac{X}{r} \\ v = -Y - R - OA + \left\{ R + r \left[1 - e^{-\frac{1}{r}(Y+OA)} \cos \frac{X}{r} \right] \right\} \cos \frac{Z}{R_0} \\ w = -Z + \left\{ R + r \left[1 - e^{-\frac{1}{r}(Y+OA)} \cos \frac{X}{r} \right] \right\} \sin \frac{Z}{R_0} \end{cases} \quad (4)$$

This kinematical model is the outcome of coupled effects generated by the longi-
200 tudinal inflexion and by the transversal deformation of cross sections. In (4), R_0
denotes the radius of the longitudinal arc that does not change its length, that
202 is, the arc whose stretch is unitary, $\lambda_Z = 1$ (*cf.* Figure 2(a)). Such a radius R_0
can be determined by using the geometric boundary condition which prescribes
204 the angle α_0 , $R_0 = L/2\alpha_0$.³ In (4), there are three other geometric quantities:
 R , r and OA . R and r are the longitudinal and transversal radii of the arc with
206 $\lambda_X = \lambda_Y = 1$ (*cf.* Figure 2(a), Figure 2(b)), respectively. Given hypothesis 2,
 r assumes the same value for all cross sections variously inclined. OA indicates
208 the ordinate at the origin of the longitudinal arc with $\lambda_X = \lambda_Y = 1$ (*cf.* Fig-
ure 2(a)). These three kinematic parameters are calculated using the following
210 three coupled expressions [1]:

$$r [a (R_0^2 - R^2) + 2bR_0^2 + c (R_0^2 + R^2)] - 2R [aR_0^2 + 3bR_0^2 + c (R_0^2 + R^2)] = 0, \quad (5)$$

$$R_0 - R = r \left(1 - \cos \frac{B}{2r} \right), \quad (6)$$

$$OA = r \ln \left[\cosh \left(\frac{H}{2r} \right) \right]. \quad (7)$$

Eqn (5) was obtained by imposing the equilibrium at the points belonging to
212 the longitudinal basic line: $X = 0$, $Y = -OA$ and $Z = Z$. The eqn (6)
was derived from the boundary conditions requiring that the lateral surface of
214 the body is unloaded. These conditions are not satisfy locally but globally.
The third expression (7) was attained on the basis of geometric considerations.
216 The positive constants a , b and c in (5) are the constitutive parameters of the

³In the sequel, the relationship between this angle α_0 and the pair of self-balanced bending moment to apply to the end faces of the beam will be found.

stored energy function ω for compressible Mooney-Rivlin materials ($\delta = \det \mathbf{F} =$
218 $\lambda_X \lambda_Y \lambda_Z$, $I_3 = \delta^2$)

$$\omega(I_1, I_2, I_3) = a I_1 + b I_2 + \Gamma(\delta), \quad (8)$$

where ⁴

$$\begin{aligned} I_1 &= \|\mathbf{F}\|^2 = \lambda_X^2 + \lambda_Y^2 + \lambda_Z^2, \\ I_2 &= \|\mathbf{F}^\star\|^2 = \lambda_X^2 \lambda_Y^2 + \lambda_X^2 \lambda_Z^2 + \lambda_Y^2 \lambda_Z^2, \\ I_3 &= (\det \mathbf{F})^2 = \lambda_X^2 \lambda_Y^2 \lambda_Z^2. \end{aligned}$$

220 In (8), $\Gamma(\delta)$ denotes a convex function that satisfies the growth conditions both
as $\delta \rightarrow 0^+$ and as $\delta \rightarrow +\infty$. For this function the expression proposed by Ciarlet
222 and Geymonat [24] has been chosen⁵

$$\Gamma(\delta) = c \delta^2 - d \ln(\delta).$$

To ensure that in the absence of deformation the stress vanishes, among the
224 four constants of ω the following relationship was established [26, 27, 28, 29]:

$$d = 2(a + 2b + c). \quad (9)$$

For further details on the displacement field (4), the reader is directly referred
226 to the paper by Lanzoni and Tarantino [1].

2.2. Numerical checks of equilibrium equations

228 Stretches can be evaluated through the definition of right Cauchy-Green
strain tensor $\mathbf{C} = \mathbf{F}^T \mathbf{F} = \mathbf{U} \mathbf{R}^{-1} \mathbf{R} \mathbf{U} = \mathbf{U}^2$, where \mathbf{R} is a proper orthogonal

⁴The following notations: $\|\mathbf{A}\| = (\text{tr} \mathbf{A}^T \mathbf{A})^{1/2}$ for the tensor norm in the linear tensor
space Lin and $\mathbf{A}^\star = (\det \mathbf{A}) \mathbf{A}^{-T}$ for the cofactor of the tensor \mathbf{A} (if \mathbf{A} is invertible) are used.

⁵For this (as for many others) constitutive models in finite elasticity it must however be
observed that they have been proposed on the basis of mathematical requirements and that
specific experimental tests, especially under multi-axial load conditions, which can validate
them are actually lacking. See for example the predictive incoherences evidenced for the
rectilinear shear deformation by Destrade et al. [25].

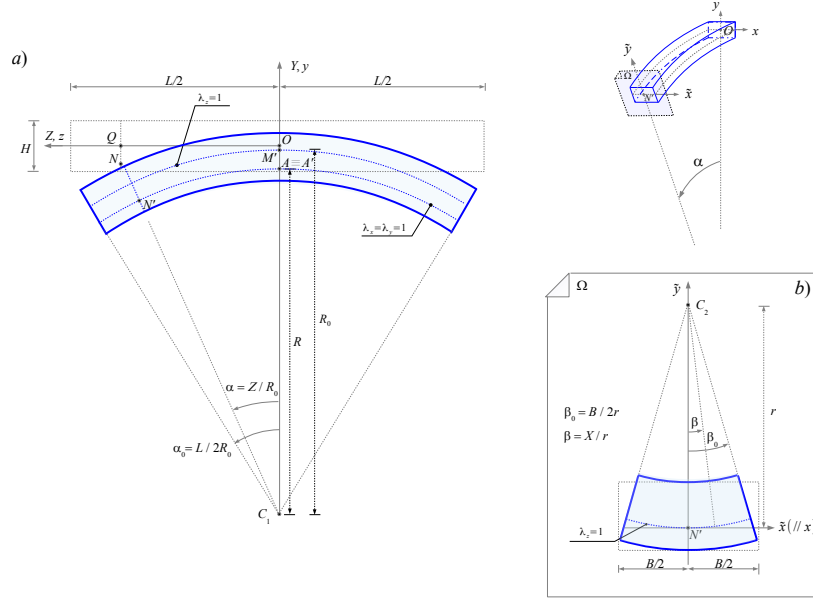


Figure 2: Deformation of the beam. a) Longitudinal deformation in the vertical YZ plane. b) Transversal deformation in the generic cross section Ω .

230 tensor that denotes the rotation tensor, whereas \mathbf{U} is a symmetric and positive
 definite tensor that indicates the right stretch tensor. As known, these two
 232 tensors are obtained by the polar decomposition of the deformation gradient
 $\mathbf{F} = \mathbf{R}\mathbf{U}$. Tensor \mathbf{U} is diagonal, because the reference system $\{O, X, Y, Z\}$
 234 is principal for the state of deformation derived from (4). Diagonal compo-
 nents of \mathbf{U} are the stretches, which are also principal. With the derivatives of
 236 the displacement field (4), the displacement gradient \mathbf{H} is obtained and then,
 through (3), the deformation gradient \mathbf{F} is derived. Once known \mathbf{F} , the right
 238 Cauchy-Green strain tensor \mathbf{C} can be evaluated using its definition. The ten-
 sor \mathbf{C} is diagonal and its diagonal components coincide with the squares of the
 240 principal stretches. Thus, the following expressions for the principal stretches

are obtained:

$$\begin{cases} \lambda_X = \lambda_Y = e^{-\frac{1}{r}(Y+OA)} \\ \lambda_Z = \frac{R+r \left[1 - e^{-\frac{1}{r}(Y+OA)} \cos \frac{X}{r} \right]}{R_0} \end{cases}, \quad (10)$$

242 taking into account that stretches are strictly positive quantities. With (10),
the deformation gradient \mathbf{F} becomes

$$[\mathbf{F}] = \begin{bmatrix} \lambda_X \cos \beta & -\lambda_Y \sin \beta & 0 \\ \lambda_X \sin \beta \cos \alpha & \lambda_Y \cos \beta \cos \alpha & -\lambda_Z \sin \alpha \\ \lambda_X \sin \beta \sin \alpha & \lambda_Y \cos \beta \sin \alpha & \lambda_Z \cos \alpha \end{bmatrix}, \quad (11)$$

244 where $\beta = X/r$ and $\alpha = Z/R_0$ are the angles shown in Figure 2. Given the
polar decomposition theorem, it is immediate to write the deformation gradient
246 (11) as product of the rotation tensor \mathbf{R} by the stretch tensor \mathbf{U} , where

$$[\mathbf{R}] = \begin{bmatrix} \cos \beta & -\sin \beta & 0 \\ \sin \beta \cos \alpha & \cos \beta \cos \alpha & -\sin \alpha \\ \sin \beta \sin \alpha & \cos \beta \sin \alpha & \cos \alpha \end{bmatrix}, \quad (12)$$

$$[\mathbf{U}] = \begin{bmatrix} \lambda_X & 0 & 0 \\ 0 & \lambda_Y & 0 \\ 0 & 0 & \lambda_Z \end{bmatrix}. \quad (13)$$

248 The constitutive law for a homogeneous, isotropic and hyperelastic material
is

$$\mathbf{T}_R = 2 \left(\frac{\partial \omega}{\partial I_1} + I_1 \frac{\partial \omega}{\partial I_2} \right) \mathbf{F} - 2 \frac{\partial \omega}{\partial I_2} \mathbf{B} \mathbf{F} + 2 I_3 \frac{\partial \omega}{\partial I_3} \mathbf{F}^{-T}, \quad (14)$$

250 where \mathbf{T}_R denotes the (first) Piola-Kirchhoff stress tensor and $\mathbf{B} = \mathbf{F} \mathbf{F}^T$ the left
Cauchy-Green strain tensor. Being $\mathbf{B} \mathbf{F} = \mathbf{R} \mathbf{U}^3$ and $\mathbf{F}^{-T} = \mathbf{R} \mathbf{U}^{-1}$, the above
252 constitutive equation can be rewritten in the following compact form:

$$\mathbf{T}_R = \mathbf{R} \mathbf{S}. \quad (15)$$

Since \mathbf{U} is diagonal (*cf.* eqn (13)), even the tensor \mathbf{S} is diagonal

$$[\mathbf{S}] = \begin{bmatrix} S_X & 0 & 0 \\ 0 & S_Y & 0 \\ 0 & 0 & S_Z \end{bmatrix},$$

254 with

$$S_J = 2 \left(\frac{\partial \omega}{\partial I_1} + I_1 \frac{\partial \omega}{\partial I_2} \right) \lambda_J - 2 \frac{\partial \omega}{\partial I_2} \lambda_J^3 + 2 I_3 \frac{\partial \omega}{\partial I_3} \frac{1}{\lambda_J}, \quad \text{for } J = X, Y, Z.$$

Equilibrium requires that the following vectorial equation must be satisfied
256 locally:

$$\text{Div } \mathbf{T}_R + \mathbf{b} = \mathbf{0}. \quad (16)$$

This vectorial equation, in the absence of body forces \mathbf{b} and after calculating
258 the scalar components of the material divergence of \mathbf{T}_R , provides a system of three partial differential equations

$$\begin{cases} - \left(\frac{S_X}{r} + S_{Y,Y} \right) \sin \frac{X}{r} + S_{X,X} \cos \frac{X}{r} = 0 \\ \left[\left(\frac{S_X}{r} + S_{Y,Y} \right) \cos \frac{X}{r} + S_{X,X} \sin \frac{X}{r} - \frac{S_Z}{R_0} \right] \cos \frac{Z}{R_0} - S_{Z,Z} \sin \frac{Z}{R_0} = 0, \\ \left[\left(\frac{S_X}{r} + S_{Y,Y} \right) \cos \frac{X}{r} + S_{X,X} \sin \frac{X}{r} - \frac{S_Z}{R_0} \right] \sin \frac{Z}{R_0} + S_{Z,Z} \cos \frac{Z}{R_0} = 0 \end{cases} \quad (17)$$

260 where $S_{J,J} = \frac{\partial S_J}{\partial J}$ for $J = X, Y, Z$ (no sum). The derivatives $S_{J,J}$ assume the following forms:

$$\begin{aligned} S_{X,X} &= 2 \left\{ \lambda_X [(\omega_{1,X} + I_{1,X} \omega_2 + I_1 \omega_{2,X}) - \omega_{2,X} \lambda_X^2] + \frac{I_{3,X} \omega_3 + I_3 \omega_{3,X}}{\lambda_X} \right\}, \\ S_{Y,Y} &= 2 \left\{ \lambda_Y [\omega_{1,Y} + I_{1,Y} \omega_2 + \omega_{2,Y} (I_1 - \lambda_Y^2)] + \lambda_{Y,Y} [\omega_1 + \omega_2 (I_1 - 3\lambda_Y^2)] \right. \\ &\quad \left. + \frac{1}{\lambda_Y} \left[\omega_3 \left(I_{3,Y} - \frac{I_3 \lambda_{Y,Y}}{\lambda_Y} \right) + I_3 \omega_{3,Y} \right] \right\}, \\ S_{Z,Z} &= 0, \end{aligned}$$

262 where $\omega_i = \frac{\partial \omega}{\partial I_i}$ for $i = 1, 2, 3$, $I_{i,K} = \frac{\partial I_i}{\partial K}$ and $\omega_{i,K} = \frac{\partial}{\partial K} \left(\frac{\partial \omega}{\partial I_i} \right)$ for $K = X, Y$, and with

$$\begin{aligned} \lambda_{Y,Y} &= \frac{\partial \lambda_Y}{\partial Y} = - \frac{e^{-\frac{1}{r}(Y+OA)}}{r}, \\ I_{1,X} &= \frac{2 \lambda_Z}{R_0} e^{-\frac{1}{r}(Y+OA)} \sin \frac{X}{r}, \\ I_{1,Y} &= 2 \left[\frac{\lambda_Z e^{-\frac{1}{r}(Y+OA)}}{R_0} \cos \frac{X}{r} - \frac{2 e^{-\frac{2}{r}(Y+OA)}}{r} \right], \\ I_{3,X} &= \frac{2 e^{-\frac{5}{r}(Y+OA)} \lambda_Z}{R_0} \sin \frac{X}{r}, \\ I_{3,Y} &= 2 \lambda_Z \left[\frac{e^{-\frac{5}{r}(Y+OA)}}{R_0} \cos \frac{X}{r} - \frac{2 \lambda_Z e^{-\frac{4}{r}(Y+OA)}}{r} \right]. \end{aligned}$$

264 Since $S_{Z,Z} = 0$, the second equation of the system (17) is multiplied by $\cos \frac{Z}{R_0}$
 and the third equation similarly by $\sin \frac{Z}{R_0}$. Now, because the two trigonometric
 266 functions $\sin \frac{Z}{R_0}$ and $\cos \frac{Z}{R_0}$ are never simultaneously zero, system (17) reduces
 to

$$\begin{cases} S_{X,X} \cos \frac{X}{r} - \left(\frac{S_X}{r} + S_{Y,Y} \right) \sin \frac{X}{r} = 0 \\ \left(\frac{S_X}{r} + S_{Y,Y} \right) \cos \frac{X}{r} + S_{X,X} \sin \frac{X}{r} - \frac{S_Z}{R_0} = 0 \end{cases}, \quad (18)$$

268 where the second equation governs the equilibrium in the Y and Z directions.
 With the stored energy function (8) for compressible Mooney-Rivlin materials,
 270 the following set of derivatives is computed:

$$\begin{aligned} \omega_1 &= a, \quad \omega_2 = b, \quad \omega_{1,X} = \omega_{1,Y} = \omega_{2,X} = \omega_{2,Y} = 0, \\ \omega_3 &= c - \frac{d}{2I_3}, \quad \omega_{3,X} = \frac{d}{R_0} \frac{e^{\frac{3}{r}(Y+OA)}}{\lambda_Z^3} \sin \frac{X}{r}, \\ \omega_{3,Y} &= -\frac{d}{\lambda_Z^2} e^{\frac{4}{r}(Y+OA)} \left[\frac{2}{r} - \frac{e^{-\frac{1}{r}(Y+OA)}}{R_0 \lambda_Z} \cos \frac{X}{r} \right]. \end{aligned} \quad (19)$$

With these derivatives, the writing of equilibrium eqns (18), derived from the
 272 displacement field (4), is completed. However, system (18) has a rather complex
 form, which makes its resolution very hard. Moreover, it must be taken in mind
 274 that, having been hypothesized *a priori* the displacement field (4), it does not
 exist the actual possibility to exactly solve the system (18) for all internal points
 276 of the body. Nevertheless, in [1] the existence of a basic longitudinal line, where
 the equilibrium eqns (18) are fully satisfied, has been recognized. The points
 278 belonging to this basic line have the following coordinates: $X = 0$, $Y = -OA$
 and $Z = Z$.

280 When the basic line is abandoned, the equilibrium equations are not fully
 satisfied. Nevertheless, it is reasonable to expect, as a result of the continuity of
 282 the displacement field, that the solution will be yet accurate in a neighbourhood
 of each single point of the basic line. To show this particular aspect of the
 284 problem, in Section 3.1, a specific numerical analysis will be performed to check
 how much the equilibrium eqns (18), assessed for any point of the cross section,
 286 move away from the zero of the basic line.

With this purpose, in the numerical analysis the geometrical dimensions of
the beam B , H and L , the angle of inflexion α_0 as well as the constitutive pa-
288 rameters a , b and c will be changed, in order to investigate the influence of
290 each parameter. In the following, the adopted units for lengths and forces are
 mm and N , respectively. These variations will be assigned starting from a ref-
292 erence beam, characterized by the following parameters: $B = H = 1$, $L = 15$,
 $\alpha_0 = \pi/3$, $a = 1$, $b = c = 0.05$. On the basis of geometrical parameters, the
294 reference beam can be considered as a realistic slender beam, that is a partic-
ularly elongated solid where the longitudinal dimension prevails considerably
296 on the two transversal dimensions. The constitutive parameters were chosen
to emphasize the term a associated with fibre length variation in the constitu-
298 tive law, rather than terms b and c corresponding to area and volume changes
(see, e.g., [30, 31]), since it plays a more important role in the deformation of a
300 realistic beam.

The geometrical dimensions of the beam, as well as the variable X , Y and
302 Z , are normalized by dividing them by H . Also the elastic constants are normal-
ized by dividing them by the first constitutive parameter a . In the sequel, the
304 same symbols will be used for both normalized and non-normalized parameters.
Having made dimensionless the elastic constants also stresses are dimension-
306 less. Consequently, the equilibrium equations become dimensionless and their
comparison with the scalar zero takes full meaning.

The results of computations are delivered in two-dimensional diagrams sim-
308 ilar to those of Figure 3, where a number of contour lines are shown. These
310 lines join the points where the equilibrium eqns (18) give the same numerical
values. A contour-plot highlights the intensity of numerical values. The white
312 colour indicates areas where the eqns (18) are practically met. The intensity of
colours grows as the difference from zero increases. Numeric results are given
314 for the particular cross section $Z = 0$, but because all cross sections deform in
the same way, they are to be considered valid for all. In these figures, the values
316 of the kinematical parameters r , R and OA , evaluated by eqns (5-7), are also
pointed out.

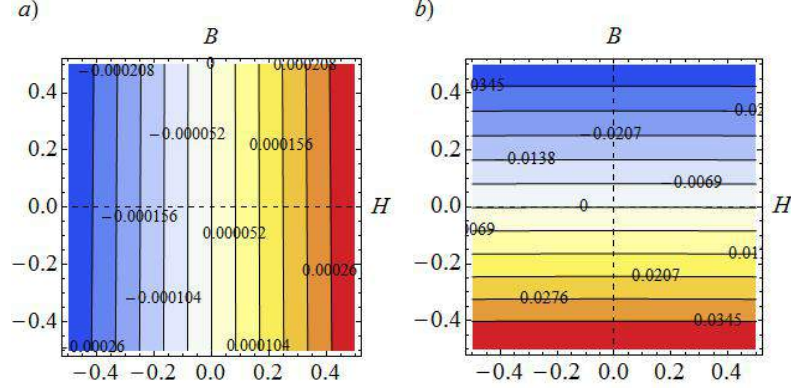


Figure 3: Plot of the equilibrium equations evaluated locally in every point belonging to the cross section $Z = 0$. Reference beam. Adopted parameters: $B = 1$, $H = 1$, $L = 15$, $\alpha_0 = \pi/3$, $a = 1$, $b = 0.05$ and $c = 0.05$. Kinematic parameters: $r = 89.3399$, $R = 7.1605$, $OA = 0.001399$. (a) Eqn (18)₁, equilibrium along the X axis. (b) Eqn (18)₂, equilibrium along the Y and Z axes.

Figure 3(a) shows the numerical results provided by eqn (18)₁ for the middle cross section ($Z = 0$) of the reference beam. As it can be noted, the numerical values are very close to zero in all points of the cross section and are exactly equal to zero for the vertical middle line ($X = 0$). The Figure 3(b) shows that the second equation of equilibrium (18)₂ is rather well satisfied along a wide horizontal band. Moving toward the upper and lower edges of the cross section, the numerical values gradually increase up to slightly exceed 4% in these edges. Such a maximum value can be considered in any case small enough and widely acceptable in many technical applications. This small discrepancy can be attributed to the second hypothesis of conservation of the planarity of cross sections and to the third hypothesis that assumes the radius r constant, since these two assumptions are not exactly verified at the edges. As a result, the elimination of this small discrepancy, having to renounce to the second and third hypotheses, may become very complicated.

For this first case examined, with a compact cross section, it can be concluded that exists a large central band, surrounding the longitudinal basic line, where the displacement field (4) can be considered accurate. The solution is a little

less precise close to the upper and lower edges of the cross section.⁶

In the following, with reference to this first case shown in Figure 3, the influence exerted by the other parameters will be investigated.

Keeping all the other parameters of the reference beam fixed, Figure 4 shows

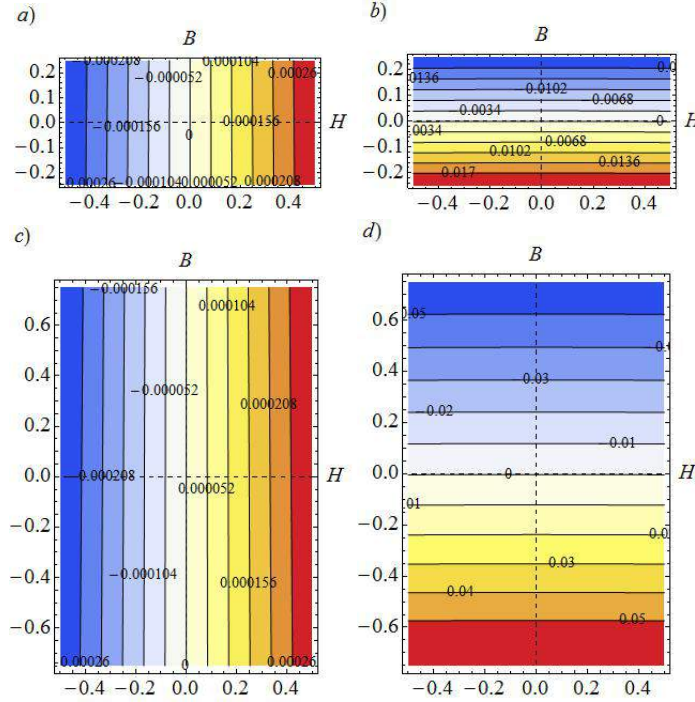


Figure 4: Plot of the equilibrium equations evaluated locally in every point belonging to the cross section $Z = 0$. Influence of the geometrical dimension H . Adopted parameters: $B = 1$, $L = 15$, $\alpha_0 = \pi/3$, $a = 1$, $b = 0.05$ and $c = 0.05$. Case with $H = 0.5$. Kinematic parameters: $r = 89.3399$, $R = 7.1605$, $OA = 0.000349$. (a) Eqn (18)₁, equilibrium along the X axis. (b) Eqn (18)₂, equilibrium along the Y and Z axes. Case with $H = 1.5$. Kinematic parameters: $r = 89.3399$, $R = 7.1605$, $OA = 0.003148$. (c) Eqn (18)₁, equilibrium along the X axis. (d) Eqn (18)₂, equilibrium along the Y and Z axes.

two cases in which the height H of the cross section is equal to $H = 0.5$ and

⁶When it is well identified the physical context in which to apply the model, then, it is possible, in order to estimate specifically the size of such a horizontal band, to define suitable confidence limits for the acceptability of the numerical solution.

340 $H = 1.5$ (in this latter case, the beam still retains a certain degree of slender-
 ness). Figures 4(a) and 4(c) show that in both cases the equilibrium equation
 342 in the X direction is practically satisfied. Height H has a greater influence on
 the equilibrium equations along the Y and Z axes. When H increases, the
 344 approximations at the upper and lower edges increase with respect to those of
 the reference beam (*cf.* Figure 4(d)), while the approximations decrease as H
 346 decreases (*cf.* Figure 4(b)).

Figure 5 shows two cases in which the base B of the cross section is equal
 to $B = 0.5$ and $B = 1.5$. The comparison of Figure 5 with Figure 3, relative to

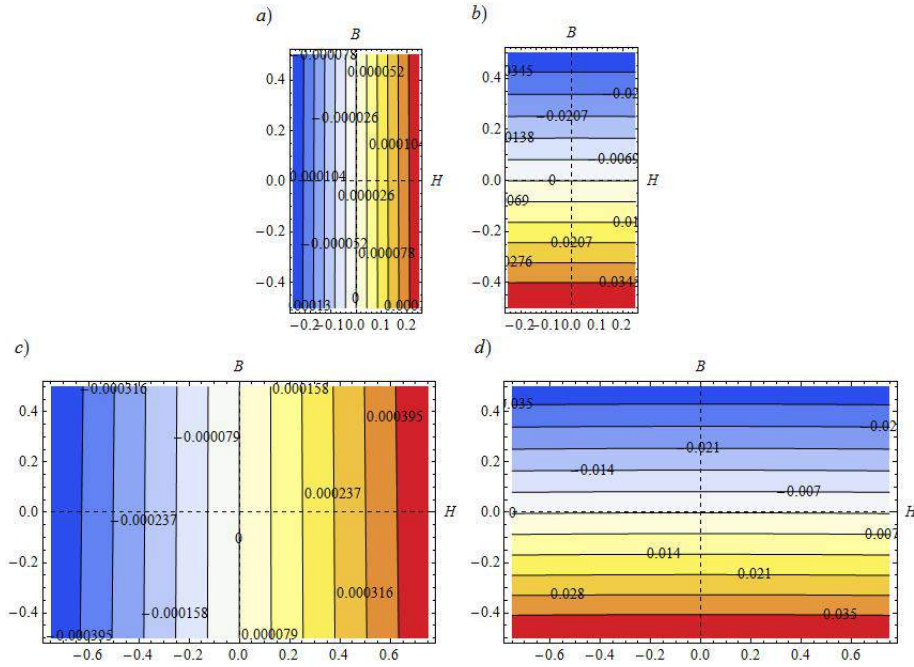


Figure 5: Plot of the equilibrium equations evaluated locally in every point belonging to
 the cross section $Z = 0$. Influence of the geometrical dimension B . Adopted parameters:
 $H = 1$, $L = 15$, $\alpha_0 = \pi/3$, $a = 1$, $b = 0.05$ and $c = 0.05$. Case with $B = 0.5$. Kinematic
 parameters: $r = 89.4785$, $R = 7.1616$, $OA = 0.001396$. (a) Eqn (18)₁, equilibrium along the
 X axis. (b) Eqn (18)₂, equilibrium along the Y and Z axes. Case with $B = 1.5$. Kinematic
 parameters: $r = 89.1091$, $R = 7.1588$, $OA = 0.001403$. (c) Eqn (18)₁, equilibrium along the
 X axis. (d) Eqn (18)₂, equilibrium along the Y and Z axes.

the reference beam, points out that the geometric dimension B does not exert an important role on the solution.

Figure 6 shows the influence of length L of the beam. If the length of the

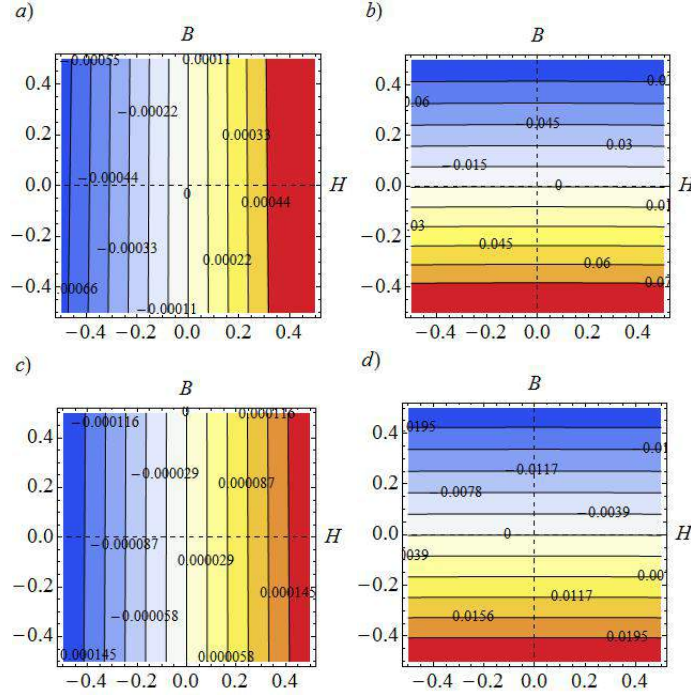


Figure 6: Plot of the equilibrium equations evaluated locally in every point belonging to the cross section $Z = 0$. Influence of the length of the beam L . Adopted parameters: $H = 1$, $B = 1$, $\alpha_0 = \pi/3$, $a = 1$, $b = 0.05$ and $c = 0.05$. Case with $L = 10$. Kinematic parameters: $r = 59.4060$, $R = 4.7725$, $OA = 0.002104$. (a) Eqn (18)₁, equilibrium along the X axis. (b) Eqn (18)₂, equilibrium along the Y and Z axes. Case with $L = 20$. Kinematic parameters: $r = 119.2277$, $R = 9.5482$, $OA = 0.001048$. (c) Eqn (18)₁, equilibrium along the X axis. (d) Eqn (18)₂, equilibrium along the Y and Z axes.

350

reference beam from $L = 15$ is reduced to $L = 10$, the errors at the edges are
 352 doubled for both equilibrium equations (*cf.* Figures 6(a) and 6(b)). Instead,
 if the length of the beam is increased to $L = 20$ then there are halved errors
 354 at the edges (*cf.* Figures 6(c) and 6(d)). Therefore the solution becomes more
 accurate as L increases, that is, in the case of very slender beams. In particular,
 356 for the last case with $L = 20$, numerical values given by (18), for all points of

the cross section, really differ little from the zero of basic line.

358 The effect of the angle of inflexion α_0 , imposed to the beam by means of the
boundary conditions, is illustrated by Figure 7. If the angle α_0 of the reference
360 beam is halved, reducing it to $\pi/6$, the values provided by the equilibrium
equations become practically zero (*cf.* Figures 7(a) and 7(b)). Conversely, the
362 approximations increase by increasing the angle α_0 (*cf.* Figures 7(c) and 7(d)).
In this last case, where the axis of the beam is inflected until to form a semi-
364 circle, errors exceed 7%. The foregoing remarks point out that the angle α_0 , as
well as the length L of the beam, plays an important role on the accuracy of
366 the solution.

Definitively, the above numerical computations show that in the cross sec-
368 tions there is a central horizontal band, where the numerical solution is accept-
able, because close to the exact solution of the longitudinal basic line. Main
approximations, due to a non complete vanishing of the equilibrium eqn (18)₂,
370 remain confined to the upper and lower edges of the cross sections. These errors
are generally small. In addition, in the case of very slender beams or in the
372 case of moderate angles α_0 , the proposed model is able to provide very accurate
374 solutions.

Figures 8 and 9 show the influence of constitutive parameters b and c .
376 When the constant b equals the constant a , errors have almost doubled (*cf.*
Figure 8(b)). A similar behaviour occurs also if the constant c grows up to one
378 (*cf.* Figure 9(b)). By way of example, for rubber-like materials, the constant b
unlikely reaches the unitary value, while the constant c can overcome the unit.

380 Figure 10 shows the non vanishing components of the Piola-Kirchhoff stress
tensor, evaluated in the middle cross section $Z = 0$ of the reference beam. For
382 this cross section, the components $T_{R,23}$, $T_{R,31}$ and $T_{R,32}$ are zero, $T_{R,11} =$
 $T_{R,22}$ and $T_{R,12} = -T_{R,21}$. Note that the out-plane component $T_{R,33}$ (*cf.* Fig-
384 ure 10(a)) is much greater than the in-plane components $T_{R,11}$, $T_{R,22}$, $T_{R,12}$
and $T_{R,21}$ (*cf.* Figures 10(b), 10(c) and 10(d)). In fact, these latter are very
386 close to zero in every point of the cross section. At the upper boundary $T_{R,33}$
assumes the maximum tensile values and at the lower boundary the maximum

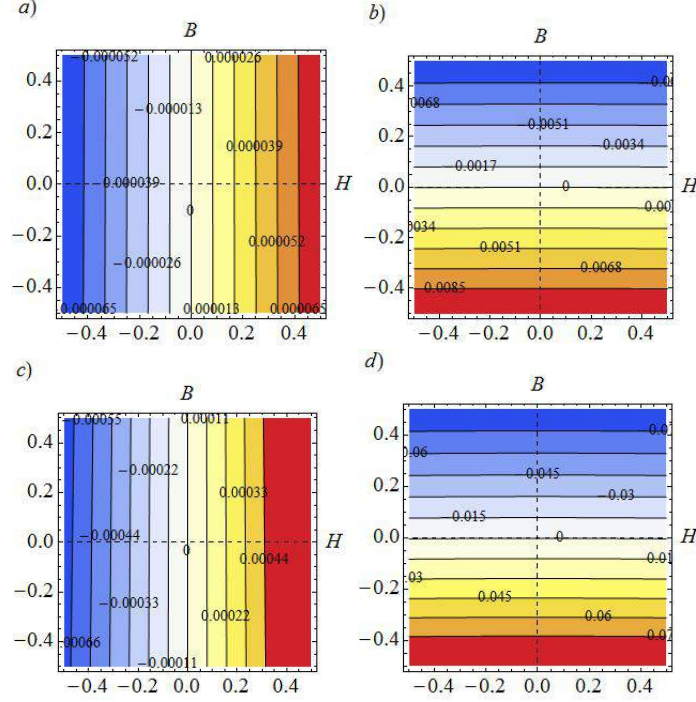


Figure 7: Plot of the equilibrium equations evaluated locally in every point belonging to the cross section $Z = 0$. Influence of the angle of inflexion α_0 . Adopted parameters: $B = 1$, $H = 1$, $L = 15$, $a = 1$, $b = 0.05$ and $c = 0.05$. Case with $\alpha_0 = \pi/6$. Kinematic parameters: $r = 178.9569$, $R = 14.3232$, $OA = 0.000698$. (a) Eqn (18)₁, equilibrium along the X axis. (b) Eqn (18)₂, equilibrium along the Y and Z axes. Case with $\alpha_0 = \pi/2$. Kinematic parameters: $r = 59.4060$, $R = 4.7725$, $OA = 0.002104$. (c) Eqn (18)₁, equilibrium along the X axis. (d) Eqn (18)₂, equilibrium along the Y and Z axes.

compression values. The curve of points with $T_{R,33} = 0$ is practically a horizontal straight line that passes very close to the centroid of the cross section. Keeping fixed the other parameters, all stress components reduce for α_0 decreasing and L increasing.

To complete the boundary-value problem that governs the equilibrium of beams, the boundary conditions must be added to the field eqns (18). The boundary conditions on the two beam bases (i.e. the two cross sections with $Z = -L/2$ and $Z = L/2$) are used to prescribe the angle α_0 . For the lateral surface of the beam, the boundary conditions can be imposed by requiring that

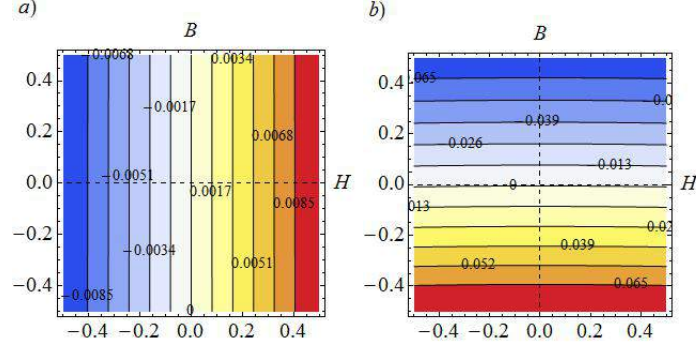


Figure 8: Plot of the equilibrium equations evaluated locally in every point belonging to the cross section $Z = 0$. Influence of the constitutive parameter b . Adopted parameters: $B = 1$, $H = 1$, $L = 15$, $a = 1$ and $c = 0.05$. Case with $b = 1$. Kinematic parameters: $r = 27.9321$, $R = 7.15749$, $OA = 0.0044741$. (a) Eqn (18)₁, equilibrium along the X axis. (b) Eqn (18)₂, equilibrium along the Y and Z axes.

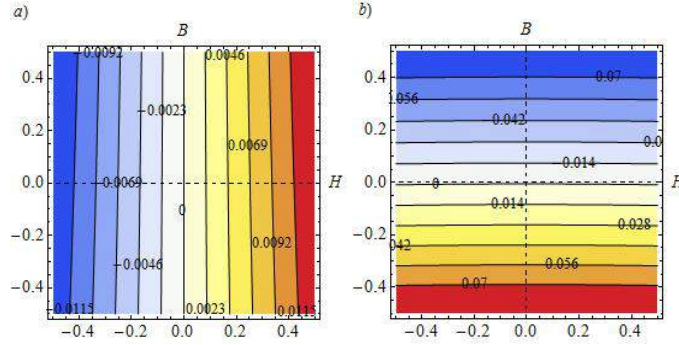


Figure 9: Plot of the equilibrium equations evaluated locally in every point belonging to the cross section $Z = 0$. Influence of the constitutive parameter c . Adopted parameters: $B = 1$, $H = 1$, $L = 15$, $a = 1$ and $b = 0.05$. Case with $c = 1$. Kinematic parameters: $r = 21.4573$, $R = 7.1561$, $OA = 0.005824$. (a) Eqn (18)₁, equilibrium along the X axis. (b) Eqn (18)₂, equilibrium along the Y and Z axes.

it is unloaded

$$\begin{aligned} \mathbf{t}_R = \mathbf{T}_R \mathbf{n} = \mathbf{0}, \quad \text{for } X = \pm \frac{B}{2}, \quad Y \in \left[-\frac{H}{2}, \frac{H}{2}\right], \quad Z \in \left[-\frac{L}{2}, \frac{L}{2}\right], \\ \text{for } Y = \pm \frac{H}{2}, \quad X \in \left[-\frac{B}{2}, \frac{B}{2}\right], \quad Z \in \left[-\frac{L}{2}, \frac{L}{2}\right], \end{aligned} \quad (20)$$

398 where \mathbf{t}_R is the Piola-Kirchhoff stress vector and \mathbf{n} is the outward unit normal.

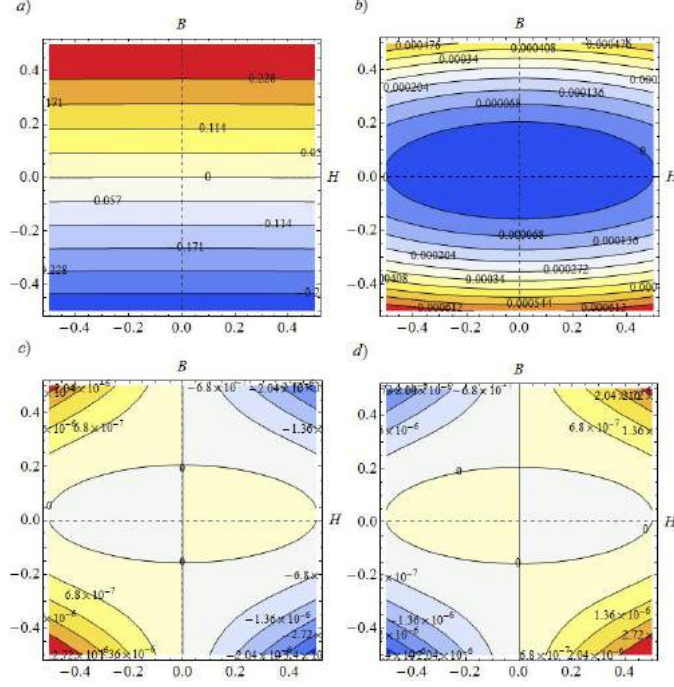


Figure 10: Plot of the components of the Piola-Kirchhoff stress tensor evaluated locally in every point belonging to the cross section $Z = 0$. Adopted parameters: $B = 1$, $H = 1$, $L = 15$, $\alpha_0 = \pi/3$, $a = 1$, $b = 0.05$ and $c = 0.05$. (a) Component $T_{R,33}$. (b) Component $T_{R,11} = T_{R,22}$. (c) Component $T_{R,12}$. (d) Component $T_{R,21}$.

Always with reference to the case considered in Figure 10, Figure 11 the stress distributions along the four sides of the cross section are plotted (for a better view of diagrams in Figure 11(b), the component $T_{R,12}$ was multiplied by a factor of 200 with respect to normal components $T_{R,11} = T_{R,22}$). Although these stress distributions are not exactly null as prescribed by boundary conditions (20), their numerical values are however very small and therefore conditions (20) may be considered approximately fulfilled.

A further check can be performed by calculating the normal force and verifying that it is close to zero. In the cross section $Z = 0$, the normal force is given by

$$N = \int T_{R,33} dA = \int_{-\frac{B}{2}}^{\frac{B}{2}} \int_{-\frac{H}{2}}^{\frac{H}{2}} S_Z dY dX, \quad (21)$$

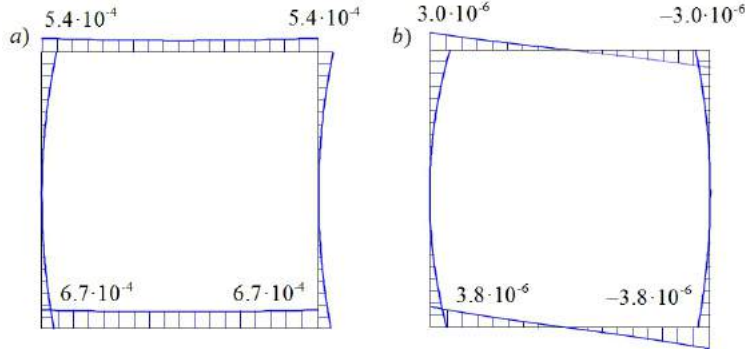
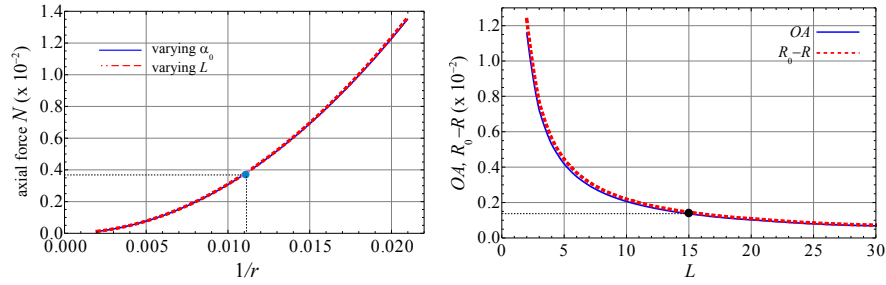


Figure 11: Plot of the stress distributions evaluated along the edges of the cross section $Z = 0$. Adopted parameters: $B = 1$, $H = 1$, $L = 15$, $\alpha_0 = \pi/3$, $a = 1$, $b = 0.05$ and $c = 0.05$. (a) Component $T_{R,11} = T_{R,22}$. (b) Component $T_{R,12} = -T_{R,21}$.

where $S_Z = 2\lambda_Z(a + 2b\lambda^2 + c\lambda^4) - \frac{d}{\lambda_Z}$ ⁷. Even the normal force N is dimensionless.

410 In Figure 12(a), N is plotted for the reference beam by varying both α_0 and L . As can be seen from Figure 12(a), N is small and it becomes even smaller when r grows.



(a) Normal force N versus the curvature $1/r$. (b) Geometrical quantities OA and $(R_0 - R)$ versus the length of the beam L .

Figure 12: Plot of the axial force N varying $1/r$ and geometrical quantities OA and $(R_0 - R)$ versus L . The dotted line represents the reference beam.

412

⁷Using (9), it can be promptly verified that in the absence of deformation ($\lambda = \lambda_Z = 1$) is $S_Z = N = 0$.

In closing this Section, we make an interesting observation. The geometrical
 414 quantities OA and $(R_0 - R)$ decrease quickly as the length of the beam L
 increases. This effect can be seen in Figure 12(b). In essence, by passing from the
 416 study of short solids [1] to that of slender beams, the two geometrical quantities
 OA and $(R_0 - R)$ lose their relevance becoming numerically very small.

418 2.3. The bending theory of slender nonlinear beams

Based on the observation carried out at the end of Section 2.2, the two
 420 geometrical quantities OA and $(R_0 - R)$, in the case of slender beams, will be
 considered identically zero. Consequently, the kinematical model illustrated in
 Figure 2 is modified as depicted by Figure 13.

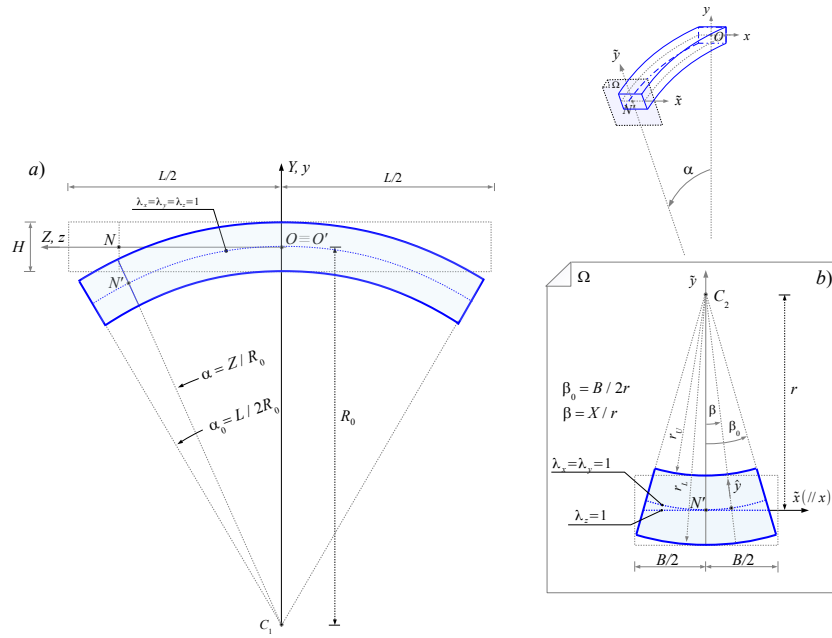


Figure 13: Deformation of a slender beam. a) Longitudinal deformation in the vertical YZ plane. b) Transversal deformation in the generic cross section Ω .

422

For slender beams, the displacement field (4) transforms into

$$\begin{cases} u = -X + r e^{-\frac{Y}{r}} \sin \frac{X}{r} \\ v = -Y - R_0 + \left[R_0 + r \left(1 - e^{-\frac{Y}{r}} \cos \frac{X}{r} \right) \right] \cos \frac{Z}{R_0} \\ w = -Z + \left[R_0 + r \left(1 - e^{-\frac{Y}{r}} \cos \frac{X}{r} \right) \right] \sin \frac{Z}{R_0} \end{cases} \quad (22)$$

424 In this system there is a single unknown kinematic parameter: the transversal radius r . It can be determined using the following relation:

$$(b + c) r - (a + 3b + 2c) R_0 = 0, \quad (23)$$

426 derived from (5). The expression (23) governs the equilibrium of the points belonging to the longitudinal basic line: $X = 0$, $Y = 0$ and $Z = Z$.⁸

428 From 22, the following expressions for the principal stretches are obtained:

$$\begin{cases} \lambda_X = \lambda_Y = e^{-\frac{Y}{r}} \\ \lambda_Z = 1 + \frac{r}{R_0} \left(1 - e^{-\frac{Y}{r}} \cos \frac{X}{r} \right) \end{cases} \quad (24)$$

Formula (11) for the deformation gradient \mathbf{F} , eqn (12) for the rotation tensor \mathbf{R} , eqn (13) for the stretch tensor \mathbf{U} and eqn (15) for the Piola-Kirchhoff stress tensor \mathbf{T}_R is still valid provided that for the stretches the expressions (24) are used.

In the deformed configuration, stretches and stresses are expressed in terms of Eulerian coordinates (x, y, z) . Using eqns (2) and (22) the Eulerian coordi-

⁸Since OA and $(R_0 - R)$ are assumed to vanish, (6) and (7) no longer serve. Indeed, in the case of slender beams, these formulae can be regarded as fulfilled because the transversal radius r is usually much larger than the dimensions B and H of the cross section. In this way, two conditions, characterized by a certain degree of approximation, are eliminated from the problem formulation.

nates of a generic point of the beam are

$$\begin{cases} x = X + u = r e^{-\frac{Y}{r}} \sin \frac{X}{r} \\ y = Y + v = -R_0 + \left[R_0 + r \left(1 - e^{-\frac{Y}{r}} \cos \frac{X}{r} \right) \right] \cos \frac{Z}{R_0} \\ z = Z + w = \left[R_0 + r \left(1 - e^{-\frac{Y}{r}} \cos \frac{X}{r} \right) \right] \sin \frac{Z}{R_0} \end{cases} \quad (25)$$

436

The inversion of this coupled system provides the following expressions:⁹

$$\begin{cases} X = r \arctan \left[\frac{x}{R_0 + r - \frac{y+R_0}{\cos \left(\arctan \frac{z}{y+R_0} \right)}} \right] \\ Y = -r \ln \left\{ \frac{R_0 + r - \frac{y+R_0}{\cos \left[\arctan \left(\frac{z}{y+R_0} \right) \right]}}{r \cos \left\{ \arctan \left(\frac{x}{R_0 + r - \frac{y+R_0}{\cos \left(\arctan \frac{z}{y+R_0} \right)}} \right) \right\}} \right\} \\ Z = R_0 \arctan \left(\frac{z}{y+R_0} \right) \end{cases} \quad (26)$$

that formally allow the transition from Lagrangian coordinates to Eulerian co-
ordinates.

438

Due to the deformation, the longitudinal basic line transforms in a arc of
circumference. The generic point N' of this curve has the following spatial
coordinates:

440

$$N' = (0, -R_0(1 - \cos \alpha), R_0 \sin \alpha), \quad (27)$$

where $\alpha = \arctan \left(\frac{z}{y+R_0} \right)$. The point N' is the origin of the reference system
(\tilde{x}, \tilde{y}) of the cross section Ω (*cf.* Figure 13(b)).

442

⁹From (25)₃ the quantity in square brackets is attained and then replaced into (25)₂, obtaining (26)₃. Similarly, from (25)₁, $r e^{-\frac{Y}{r}}$ is evaluated and then substituted into (25)₂, obtaining (26)₁. Expression (26)₂ is evaluated directly from (25)₂ using (26)₁ and (26)₃.

444 Substituting (26) into (24), the principal stretches λ_x , λ_y and λ_z are obtained

$$\begin{cases} \lambda_x = \lambda_y = \frac{R_0 + r - \frac{y+R_0}{\cos\left[\arctan\left(\frac{z}{y+R_0}\right)\right]}}{r \cos\left(\arctan\left[\frac{x}{R_0 + r - \frac{y+R_0}{\cos\left(\arctan\left(\frac{z}{y+R_0}\right)\right)}}\right]\right)} \\ \lambda_z = 1 + \frac{1}{R_0} \left\{ \frac{y+R_0}{\cos\left[\arctan\left(\frac{z}{y+R_0}\right)\right]} - R_0 \right\} \end{cases} . \quad (28)$$

These Eulerian expressions are more complicated than the corresponding Lagrangian ones. In particular, while stretches $\lambda_X = \lambda_Y$ depend only on the material variable Y , now, in the deformed configuration, the corresponding stretches $\lambda_x = \lambda_y$ depend on all three spatial variables x , y and z . Note also that λ_z loses the dependence on spatial variable x .

450 As shown in Figure 13(b), for the generic cross section Ω , the stretch λ_z is unitary along the horizontal straight line passing through N' . This line ($\tilde{y} = 0$)
452 can be considered as the neutral axis for the deformation. Moreover, λ_z has the same diagram along all vertical straight lines of cross section Ω , that is
454 by varying the abscissa \tilde{x} and holding the α angle fixed. The shape of such a vertical diagram is linear in \tilde{y}

$$\lambda_z = 1 + \frac{\tilde{y}}{R_0}. \quad (29)$$

456 This simple and compact formula is obtained by introducing the variable $\tilde{y} = \frac{y+R_0}{\cos \alpha} - R_0$ into (28)₂.

458 It is important to note that the linear laws obtained for the stretch λ_z and for its neutral axis are direct consequences of the kinematic model adopted. In
460 fact, given the hypothesis of the planarity preservation for cross sections, all cross sections of the beam deform maintaining own plane and rotating around
462 the neutral axis. The rotation is finite. This kind of deformation leads directly to expression (29) for the longitudinal stretch λ_z in the deformed configuration.

464 The stretches $\lambda_x = \lambda_y$ are unitary along the circle arc with radius r , concavity upwards and passing through the point N' (*cf.* Figure 13(b)). Even for
466 these stretches it is possible to obtain a simple and compact expression such as

(29). In fact, using \tilde{y} and introducing the new variable $\hat{y} = \frac{\tilde{y} - r(1 - \cos \beta)}{\cos \beta}$, where
 468 $\beta = \arctan\left(\frac{x}{r - \tilde{y}}\right)$, (28)₁ transforms into

$$\lambda_x = \lambda_y = 1 - \frac{\hat{y}}{r}. \quad (30)$$

As shown by this equation, the transversal stretches $\lambda_x = \lambda_y$ are linear along
 470 the \hat{y} direction. In addition, their diagrams are the same as themselves along
 the curved cross section profile. That is, they are the same for each β angle.

472 To apply formulae (29) and (30) the coordinates \tilde{y} and \hat{y} for each point of
 the deformed beam can be evaluated by using (25), whereas the radius R_0 is
 474 given by the boundary conditions and the radius r can be computed directly
 from (23).

476 Figure 14 shows a comparison between Lagrangian and Eulerian stretches
 evaluated for the middle cross section of a slender beam. To emphasize the

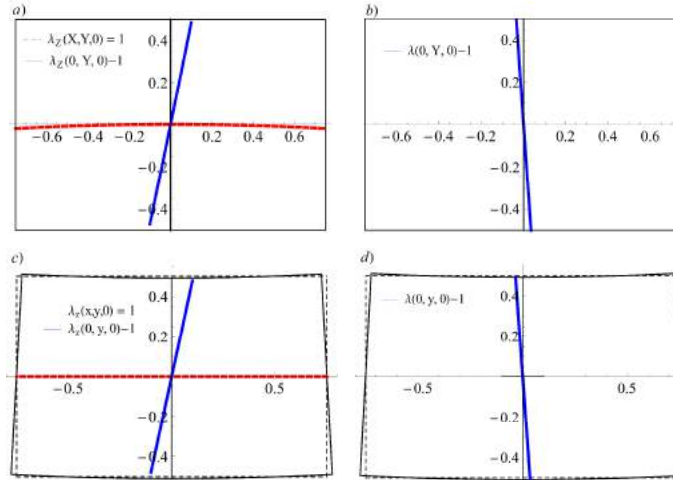


Figure 14: Diagrams of the stretches minus one along the vertical lines $x = X = 0$ of the middle cross section of a slender beam. Adopted parameters: $B = 3/2$, $H = 1$, $L = 15$, $\alpha_0 = \pi/2$, $a = b = c = 1$. Longitudinal and transversal stretches in the reference configuration. (a) $\lambda_Z - 1$. (b) $\lambda_X - 1 = \lambda_Y - 1$. Longitudinal and transversal stretches in the deformed configuration. (c) $\lambda_z - 1$. (d) $\lambda_x - 1 = \lambda_y - 1$.

478 anticlastic effect, the two constitutive constants b and c were set equal to one.
 To distinguish between dilations and contractions, in this figure the functions
 480 $(\lambda - 1)$ are plotted. The cross section is thus divided into two parts by the line
 $\lambda = 1$. In the part where $(\lambda - 1)$ is positive there is dilatation and in the other
 482 part, where $(\lambda - 1)$ is negative, there is contraction. For the vertical line $X = 0$ of
 the middle cross section of the undeformed beam, in Figure 14(a) and 14(b) the
 484 diagrams of $(\lambda_Z - 1)$ and $(\lambda_X - 1)$ are drawn. These functions were obtained by
 using (24) and they show a quasi-rectilinear shape, since the exponent $(-Y/r)$ of
 486 the exponential function is a small quantity. In Figure 14(a), with a dotted line,
 the curve $\lambda_Z = 1$ is displayed. This curve, which shows the concavity facing
 488 downward, after the inflexion of the beam will become perfectly straight (*cf.*
 Figure 14(c)). Figure 14(c) and 14(d) show the functions $(\lambda_z - 1)$ and $(\lambda_x - 1)$
 490 in the deformed cross section. The Eulerian stretches (28) for $x = z = 0$, or
 equivalently (29) and (30) for $\alpha = \beta = 0$, provide the following liner expressions:

$$\begin{cases} \lambda_x = \lambda_y = 1 - \frac{y}{r} \\ \lambda_z = 1 + \frac{y}{R_0} \end{cases}, \quad (31)$$

492 which were used to plot Figures 14(c) and 14(d).

Considering the longitudinal profile of the inflexed beam, in Figure 15 some
 494 diagrams of $(\lambda_z - 1)$ are shown for discrete values of the variable z . The stretch
 λ_z is evaluated by $(28)_2$. The parameters adopted are those of the beam of
 496 Figure 14. As can be noted in Figure 15, for all cross sections the same linear
 diagram is obtained. At the upper fibre, $\lambda_{z,max} = 1.1029$, while at the lower
 498 fibre $\lambda_{z,min} = 0.8934$. Obviously, this result is immediately apparent from (29)
 which predicts the same diagram for each α angle.

500 In the sequel, using the results obtained so far, some geometrical quantities
 of the beam in the deformed configuration are computed. The radii of curvature
 502 of the lower (r_L) and upper (r_U) fibres of the cross section after bending (*cf.*
 Figure 13) turn out to be ($r_L > r_U$)

$$r_L = r + \int_{-\frac{H}{2}}^0 \lambda_Y(\hat{Y}) d\hat{Y} = r e^{\frac{H}{2r}}, \quad r_U = r - \int_0^{\frac{H}{2}} \lambda_Y(\hat{Y}) d\hat{Y} = r e^{-\frac{H}{2r}}. \quad (32)$$

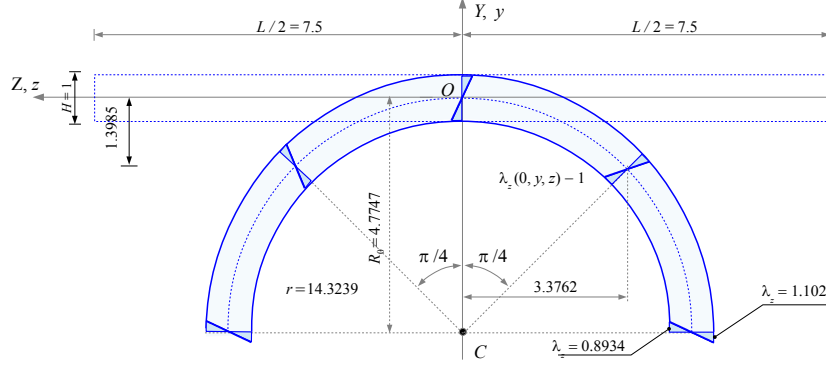


Figure 15: Longitudinal distribution of diagrams $(\lambda_z - 1)$ in the deformed configuration.

504 The difference between these two radii is the radial thickness

$$H' = 2r \sinh\left(\frac{H}{2r}\right), \quad (33)$$

which is constant. Knowing the external radii r_L and r_U it is possible to evaluate
506 the area of the deformed cross section A' as

$$A' = \int_{-\beta_0}^{\beta_0} d\vartheta \int_{r_U}^{r_L} \rho d\rho = 2r^2 \beta_0 \sinh\left(\frac{H}{r}\right), \quad (34)$$

where (ρ, ϑ) is a polar coordinate system with pole at the point C_2 of Fig-
508 ure 13(b). The distance between the centroid G of the deformed cross section
and the pole C_2 is

$$C_2 G = \frac{1}{A'} \int_{-\beta_0}^{\beta_0} \cos \vartheta d\vartheta \int_{r_U}^{r_L} \rho^2 d\rho = \frac{2}{3} r \frac{\sin \beta_0}{\beta_0} \frac{\sinh\left(\frac{3H}{2r}\right)}{\sinh\left(\frac{H}{r}\right)}. \quad (35)$$

510 According to the second Pappus-Guldinus theorem, the volume of the inflexed
beam V' can be calculated as the volume of revolution generated by the ro-
512 tation of A' around C_1 . Thus, with (34) and (35), the following expression is

obtained:¹⁰

$$\begin{aligned} V' &= 2\alpha_0(R_0 + r - C_2 G) A' \\ &= \frac{4}{3}\alpha_0 r^2 \left[3\beta_0(R_0 + r) - 2r \frac{\sinh\left(\frac{3H}{2r}\right)}{\sinh\left(\frac{H}{r}\right)} \sin\beta_0 \right] \sinh\left(\frac{H}{r}\right). \end{aligned} \quad (36)$$

Let us now consider the stresses. Lagrangian stresses are expressed by the Piola-Kirchhoff stress tensor \mathbf{T}_R (*cf.* eqn (15)). The stress measure coherently employed in the spatial configuration is instead that of Cauchy. The Cauchy stress tensor \mathbf{T} is obtained from the Piola-Kirchhoff stress tensor \mathbf{T}_R through the well-known transformation

$$\mathbf{T}_R = \mathbf{T} \mathbf{F}^*. \quad (37)$$

Using (11), (12), (13), (15) and (37), the following components of the Cauchy stress tensor are computed ($S = S_X = S_Y$, $\lambda = \lambda_X = \lambda_Y$):

$$\lambda^2 \lambda_Z [\mathbf{T}] = \begin{bmatrix} S\lambda & 0 & 0 \\ 0 & S\lambda \cos^2 \alpha + S_Z \lambda_Z \sin^2 \alpha & (S\lambda - S_Z \lambda_Z) \sin \alpha \cos \alpha \\ 0 & (S\lambda - S_Z \lambda_Z) \sin \alpha \cos \alpha & S\lambda \sin^2 \alpha + S_Z \lambda_Z \cos^2 \alpha \end{bmatrix}, \quad (38)$$

being $\mathbf{F}^* = (\lambda^2 \lambda_Z) \mathbf{R} \mathbf{U}^{-1}$ and $(\lambda^2 \lambda_Z) \mathbf{T} = \mathbf{R} \mathbf{S} \mathbf{U} \mathbf{R}^T$. The tensor \mathbf{T} is symmetric. The matrix (38) can be rewritten in diagonal form by evaluating its eigenvalues. The resolution of the characteristic polynomial allows the determination of the principal Cauchy stresses

$$[\mathbf{T}] = \begin{bmatrix} \frac{S}{\lambda \lambda_Z} & 0 & 0 \\ 0 & \frac{S}{\lambda \lambda_Z} & 0 \\ 0 & 0 & \frac{S_Z}{\lambda^2} \end{bmatrix}, \quad (39)$$

where

$$\begin{aligned} T_1 = T_2 &= \frac{S}{\lambda \lambda_Z} = \frac{2}{\lambda_Z} [\omega_1 + (\lambda^2 + \lambda_Z^2) \omega_2 + \lambda^2 \lambda_Z^2 \omega_3], \\ T_3 &= \frac{S_Z}{\lambda^2} = \frac{2\lambda_Z}{\lambda^2} (\omega_1 + 2\lambda^2 \omega_2 + \lambda^4 \omega_3). \end{aligned} \quad (40)$$

¹⁰It can be seen that, by taking $B = 2\beta_0 r$, (34) reduces to BH as $r \rightarrow \infty$. Similarly, by taking $L = 2\alpha_0 R_0$, (36) becomes $V' = BHL$ as $(R_0, r) \rightarrow \infty$.

526 The principal directions of stress are the eigenvectors associated with these
eigenvalues. The principal direction corresponding to the eigenvalue T_3 is the
528 unit vector orthogonal to the plane Ω (*cf.* Figure 13) with components $(0,$
 $-\sin \alpha, \cos \alpha)$. The others two eigenvectors are any two unit vectors orthogonal
530 to each other and belonging to the plane Ω . Substituting (9) and (19) in (40),
the principal Cauchy stresses for a compressible Mooney-Rivlin material are
532 obtained

$$\begin{aligned} T_1 = T_2 &= \frac{2}{\lambda^2 \lambda_Z} \{ (\lambda^2 - 1) a + [(\lambda^2 + \lambda_Z^2) \lambda^2 - 2] b + (\lambda^4 \lambda_Z^2 - 1) c \}, \\ T_3 &= \frac{2}{\lambda^2 \lambda_Z} [(\lambda_Z^2 - 1) a + 2(\lambda^2 \lambda_Z^2 - 1) b + (\lambda^4 \lambda_Z^2 - 1) c]. \end{aligned} \quad (41)$$

Note that in the absence of deformation these stresses vanish. To represent
534 stresses in the deformed configuration is necessary to use the expressions (28)
for the stretches.

536 Figure 16 shows a comparison between Piola-Kirchhoff and Cauchy stresses
evaluated, locally in every point belonging to the middle cross section of the
538 beam, in the undeformed and deformed configuration, respectively. Piola-
Kirchhoff stresses are calculated using (15) with $\alpha = 0$ and Cauchy stresses by
540 (38) still for $\alpha = 0$. As can be seen from this figure, the longitudinal stress com-
ponents $T_{R,33}$ and T_{33} are considerably greater than the in-plane components,
542 which are close to zero. Furthermore, for the longitudinal stress components,
the following can be observed. In the upper half of the cross section there are
544 tensile stresses and in the lower one there are compression stresses. In absolute
value, maximum levels of stress are reached at the upper and lower edges (*cf.*
546 Figures 16(a) and 16(c)). Figure 17 continues to provide information on the
stresses shown in Figure 16, but it is now organized as Figure 14, previously
548 plotted for stretches. Figure 17 shows the diagrams of the stress along the ver-
tical lines $X = Z = 0$ and $x = z = 0$. To compute Piola-Kirchhoff stresses,
550 which are principal, eqn (15) with $\alpha = \beta = 0$ has been used. The Cauchy prin-
cipal stresses are calculated by using (41). Though the corresponding stretch
552 diagrams of Figures 14(c) and 14(d) are linear, the diagrams of Figures 17(c)
and 17(d) are nonlinear. In Figure 17(c), with a dashed line, the neutral line for

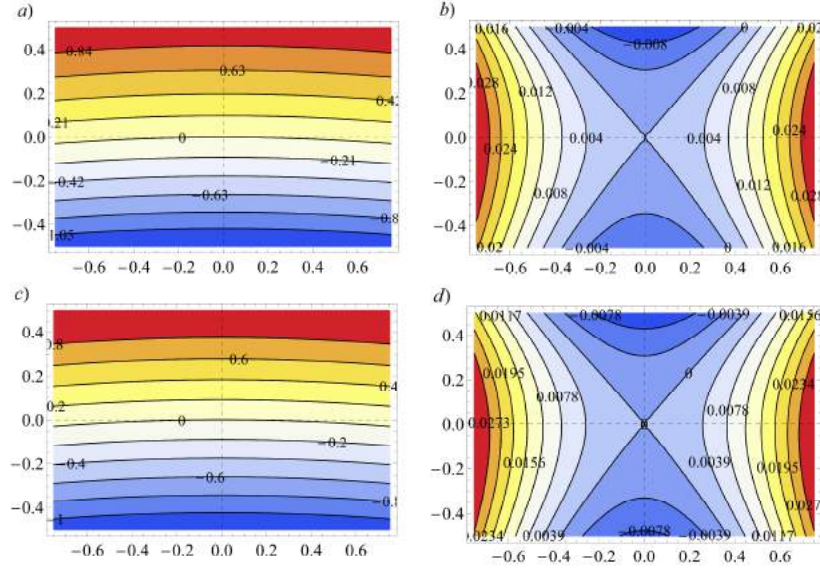


Figure 16: Plot of the components of the stress evaluated locally in every point belonging to the middle cross section $Z = z = 0$ of a slender beam. Adopted parameters: $B = 3/2$, $H = 1$, $L = 15$, $\alpha_0 = \pi/2$, $a = b = c = 1$. Piola-Kirchhoff stresses. (a) Component $T_{R,33}$. (b) Components $T_{R,11} = T_{R,22}$. Cauchy stresses. (c) Component T_{33} . (d) Components $T_{11} = T_{22}$.

554 which $T_3 = 0$ is also pointed out. Although the two lines are near, the neutral
 556 $\lambda_z = 0$.
 curve for the stresses does not coincide with the neutral axis for the deformation

The longitudinal diagrams of the Cauchy principal stress T_3 are shown in
 558 Figure 18. As in the case of the stretches illustrated by Figure 15, the stress
 diagrams are all equal along the curved profile of the beam. At the upper fibre,
 560 $T_3 = 1.05606$ (tensile), while at the lower fibre $T_3 = -1.19428$ (compression).

Knowing the stress distributions, the normal force n and the bending mo-
 562 ment m_x can be evaluated. Using the polar coordinate system (ρ, β) of Fig-
 ure 13(b), for the generic deformed cross section Ω the following expressions are
 564 derived:

$$n = \int_{-\beta_0}^{\beta_0} \int_{\rho_{min}}^{\rho_{max}} \rho T_3(\rho, \beta) d\rho d\beta, \quad m_x = \int_{-\beta_0}^{\beta_0} \int_{\rho_{min}}^{\rho_{max}} \rho T_3(\rho, \beta) \tilde{y} d\rho d\beta, \quad (42)$$

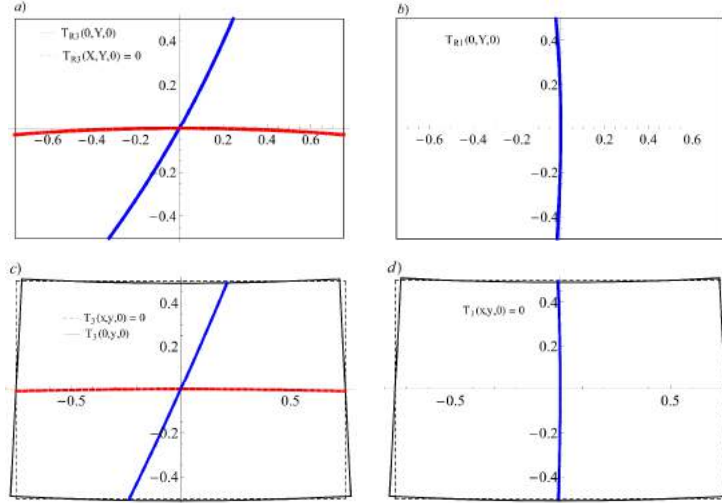


Figure 17: Diagrams of principal stresses along the vertical lines $x = X = 0$ of the middle cross section of a slender beam. Adopted parameters: $B = 3/2$, $H = 1$, $L = 15$, $\alpha_0 = \pi/2$, $a = b = c = 1$. Piola-Kirchhoff stresses. (a) Component $T_{R,3}$. (b) Components $T_{R,1} = T_{R,2}$. Cauchy stresses. (c) Component T_3 . (d) Components $T_1 = T_2$.

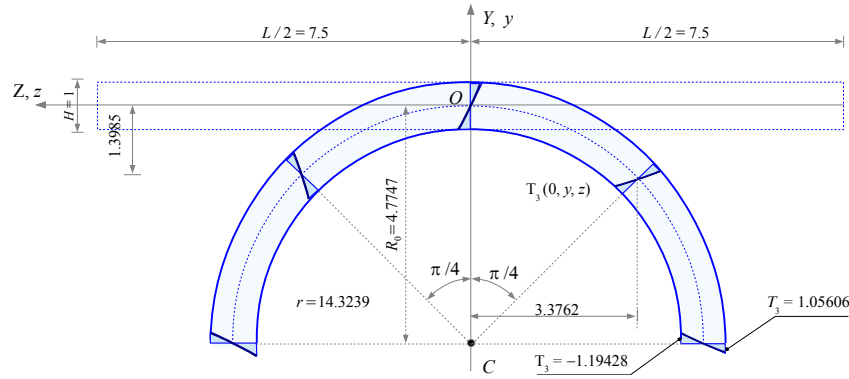


Figure 18: Longitudinal distribution of diagrams of Cauchy principal stress T_3 in the deformed configuration.

where $\tilde{x} = \rho \sin \beta$, $\tilde{y} = r - \rho \cos \beta$, $\rho_{min} = r_U = r e^{-\frac{H}{2r}}$, $\rho_{max} = r_L = r e^{\frac{H}{2r}}$.

566 The modulus of the above internal actions does not depend on the cross section

Ω .

568 In terms of polar coordinates (ρ, β) , the stretches (28), for the middle cross section $z = 0$, assume the following form:

$$\begin{cases} \lambda = \lambda_x = \lambda_y = \frac{\rho}{r} \\ \lambda_z = 1 + \frac{r - \rho \cos \beta}{R_0} \end{cases} \quad (43)$$

570 Substituting (41)₂ and (43) into (42)₁, the normal force n is obtained as the sum of four integrals

$$\begin{aligned} 2a \int_{-\beta_0}^{\beta_0} \int_{\rho_{min}}^{\rho_{max}} \frac{\lambda_z}{\lambda^2} \rho d\rho d\beta &= 2a \left(1 + \frac{r}{R_0}\right) BH - 8a \frac{r^3}{R_0} \sinh\left(\frac{H}{2r}\right) \sin\left(\frac{B}{2r}\right), \\ 4b \int_{-\beta_0}^{\beta_0} \int_{\rho_{min}}^{\rho_{max}} \lambda_z \rho d\rho d\beta &= 4b \left(1 + \frac{r}{R_0}\right) rB \sinh\left(\frac{H}{r}\right) - \frac{16}{3} b \frac{r^3}{R_0} \sinh\left(\frac{3H}{2r}\right) \sin\left(\frac{B}{2r}\right), \\ 2c \int_{-\beta_0}^{\beta_0} \int_{\rho_{min}}^{\rho_{max}} \lambda^2 \lambda_z \rho d\rho d\beta &= c \left(1 + \frac{r}{R_0}\right) rB \sinh\left(\frac{2H}{r}\right) - \frac{8c}{5} \frac{r^3}{R_0} \sinh\left(\frac{5H}{2r}\right) \sin\left(\frac{B}{2r}\right), \\ - (2a + 4b + 2c) \int_{-\beta_0}^{\beta_0} \int_{\rho_{min}}^{\rho_{max}} \frac{\rho}{\lambda^2 \lambda_z} d\rho d\beta &= - (2a + 4b + 2c) \frac{rR_0}{(r + R_0)} \left\{ \frac{BH}{r} \right. \\ &\quad \left. - B \ln \left[\frac{r + R_0 - r e^{\frac{H}{2r}}}{r + R_0 - r e^{-\frac{H}{2r}}} \right] + \frac{(r + R_0) B^3 \sinh\left(\frac{H}{2r}\right)}{12r \left[2r(r + R_0) \cosh\left(\frac{H}{2r}\right) - (2r^2 + 2rR_0 + R_0^2) \right]} \right\}. \end{aligned} \quad (44)$$

572 Similarly, the bending moment m_x is provided by the sum of the following four integrals:

$$\begin{aligned} 2a \int_{-\beta_0}^{\beta_0} \int_{\rho_{min}}^{\rho_{max}} \frac{\lambda_z}{\lambda^2} (r - \rho \cos \beta) \rho d\rho d\beta &= 2a \left(1 + \frac{r}{R_0}\right) rBH \\ &\quad - 8a \left(1 + \frac{2r}{R_0}\right) r^3 \sinh\left(\frac{H}{2r}\right) \sin\left(\frac{B}{2r}\right) + a \frac{r^4}{R_0} \sinh\left(\frac{H}{r}\right) \left[\sin\left(\frac{B}{r}\right) + \frac{B}{r} \right], \\ 4b \int_{-\beta_0}^{\beta_0} \int_{\rho_{min}}^{\rho_{max}} \lambda_z (r - \rho \cos \beta) \rho d\rho d\beta &= 4b \left(1 + \frac{r}{R_0}\right) r^2 B \sinh\left(\frac{H}{r}\right) \\ &\quad - \frac{16}{3} b \left(1 + \frac{2r}{R_0}\right) r^3 \sinh\left(\frac{3H}{2r}\right) \sin\left(\frac{B}{2r}\right) + b \frac{r^4}{R_0} \sinh\left(\frac{2H}{r}\right) \left[\sin\left(\frac{B}{r}\right) + \frac{B}{r} \right], \\ 2c \int_{-\beta_0}^{\beta_0} \int_{\rho_{min}}^{\rho_{max}} \lambda^2 \lambda_z (r - \rho \cos \beta) \rho d\rho d\beta &= c \left(1 + \frac{r}{R_0}\right) r^2 B \sinh\left(\frac{2H}{r}\right) \\ &\quad - \frac{8}{5} c \left(1 + \frac{2r}{R_0}\right) r^3 \sinh\left(\frac{5H}{2r}\right) \sin\left(\frac{B}{2r}\right) + \frac{1}{3} c \frac{r^4}{R_0} \sinh\left(\frac{3H}{r}\right) \left[\sin\left(\frac{B}{r}\right) + \frac{B}{r} \right], \\ - (2a + 4b + 2c) \int_{-\beta_0}^{\beta_0} \int_{\rho_{min}}^{\rho_{max}} \frac{1}{\lambda^2 \lambda_z} (r - \rho \cos \beta) \rho d\rho d\beta &= - (2a + 4b + 2c) \left\{ \frac{rR_0 B}{(r + R_0)} \left[H \right. \right. \\ &\quad \left. \left. - R_0 \ln \left(\frac{r + R_0 - r e^{-\frac{H}{2r}}}{r + R_0 - r e^{\frac{H}{2r}}} \right) \right] - \frac{R_0^2 B^3 \left(e^{\frac{H}{r}} - 1 \right)}{24 \left[\left(e^{\frac{H}{2r}} - 1 \right) r - R_0 \right] \left[\left(e^{\frac{H}{2r}} - 1 \right) r + R_0 e^{\frac{H}{2r}} \right]} \right\}. \end{aligned} \quad (45)$$

574 To simplify the calculus of integrals (44)₄ and (45)₄, after the first integration in the variable ρ , the integrand functions have been developed in power series around $\beta = 0$, taking into account the powers up to β^2 .

As the corresponding Lagrangian normal force N (*cf.* Figure 12(a)), the
 578 Eulerian normal force n , assessed by (42)₁ and (44), is small and becomes even
 smaller for L increasing.

580 Expression (42)₂, with integrals (45), can be thought of as the moment-
 curvature relationship for nonlinear beams, $m_x = \hat{m}_x(R_0^{-1})$. In addition, since
 582 $\alpha_0 = L/2R_0$, the (42)₂ can also be used to establish the correspondence between
 the moment m_x and the angle α_0 . Pursuing this goal, the diagram plotted in
 584 Figure 19 has been obtained for the beam considered in Figures 14-18. In this
 last figure, the moment m_x is assessed numerically by varying the angle α_0 . On
 586 the basis of this result, the boundary conditions at the two end faces can be set
 geometrically by means of the angle α_0 or statically through the application of
 588 the corresponding moment m_x .

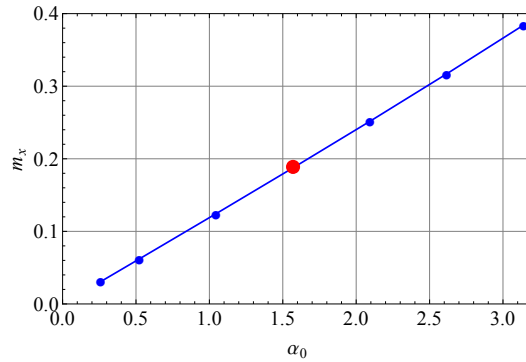


Figure 19: Plot of the bending moment m_x versus the angle α_0 .

2.4. Linearization

590 Enforcing the hypotheses of smallness of both the deformation and displace-
 ment fields, the theory exposed in Section 2.3 will be linearized, retrieving the
 592 classical results of the linear theory of inflexed beams. For this purpose, the
 main formulae will develop in power series as functions of the radii r and R_0 .
 594 These series will be truncated preserving the infinitesimals of order $\mathcal{O}(r^{-1})$ and
 $\mathcal{O}(R_0^{-1})$ as $r \rightarrow \infty$ or $R_0 \rightarrow \infty$. Therefore, the displacement field (22) can be

596 approximated as ¹¹

$$\begin{aligned}
u &\simeq -X + r \left[1 - \frac{Y}{r} + \frac{Y^2}{2r^2} + o(r^{-2}) \right] \left[\frac{X}{r} + o(r^{-2}) \right] \simeq -\frac{XY}{r} + o(r^{-1}), \\
v &\simeq -Y - R_0 + \left\{ R_0 + r - r \left[1 - \frac{Y}{r} + \frac{Y^2}{2r^2} + o(r^{-2}) \right] \left[1 - \frac{X^2}{2r^2} + o(r^{-3}) \right] \right\} \\
&\quad \left[1 - \frac{Z^2}{2R_0^2} + o(R_0^{-3}) \right] \simeq -\frac{Y^2}{2r} + \frac{X^2}{2r} - \frac{Z^2}{2R_0} + o(r^{-1}) + o(R_0^{-1}), \\
w &\simeq -Z + \left\{ R_0 + r - r \left[1 - \frac{Y}{r} + \frac{Y^2}{2r^2} + o(r^{-2}) \right] \left[1 - \frac{X^2}{2r^2} + o(r^{-3}) \right] \right\} \\
&\quad \left[\frac{Z}{R_0} + o(R_0^{-2}) \right] \simeq \frac{YZ}{R_0} + o(r^{-1}) + o(R_0^{-1}),
\end{aligned} \tag{46}$$

having neglected the infinitesimal terms of higher order than r^{-1} and R_0^{-1} . In
598 the linearized theory of inflexed beams, the following two well-known relationships hold:

$$\frac{1}{R_0} = \frac{M_X}{E J_X}, \quad r = \frac{R_0}{\nu}, \tag{47}$$

600 where M_X denotes the bending moment around the X axis, J_X the moment of
inertia of the cross section with respect to the X axis, E the Young modulus
602 and ν the Poisson ratio. The first equation represents the moment-curvature
relationship and the second equation is derived from the ratio between the longitudinal and transversal radii. Introducing eqn (47) into (46), the infinitesimal
604 displacement field is lastly derived¹²

$$\begin{cases} u \simeq -\frac{\nu M_X}{E J_X} XY \\ v \simeq \frac{1}{2} \frac{M_X}{E J_X} [\nu(X^2 - Y^2) - Z^2] \\ w \simeq \frac{M_X}{E J_X} YZ \end{cases}, \tag{48}$$

¹¹The Landau symbols are used. In addition, in eqn (46) using the Taylor series expansions, the following approximations are employed:

$$\begin{aligned}
e^{-\frac{Y}{r}} &\simeq 1 - \frac{Y}{r} + \frac{Y^2}{2r^2} + o(r^{-2}), \quad \sin \frac{X}{r} \simeq \frac{X}{r} + o(r^{-2}), \\
\cos \frac{X}{r} &\simeq 1 - \frac{X^2}{2r^2} + o(r^{-3}), \quad \sin \frac{Z}{R_0} \simeq \frac{Z}{R_0} + o(R_0^{-2}), \\
\cos \frac{Z}{R_0} &\simeq 1 - \frac{Z^2}{2R_0^2} + o(R_0^{-3}).
\end{aligned}$$

¹²In the sequel, the infinitesimal terms of higher order are omitted definitively.

in the classic form which can be found in any textbook.

The linearization of the stretches (24) gives

$$\begin{cases} \lambda_X = \lambda_Y \simeq 1 - \frac{Y}{r} \\ \lambda_Z \simeq 1 + \frac{Y}{R_0} \end{cases}, \quad (49)$$

and, subsequently, the deformation gradient \mathbf{F} (11), the rotation tensor \mathbf{R} (12) and the stretch tensor \mathbf{U} (13) transform into

$$\begin{aligned} [\mathbf{F}] &\simeq \begin{bmatrix} 1 - \frac{Y}{r} & -\frac{X}{r} & 0 \\ \frac{X}{r} & 1 - \frac{Y}{r} & -\frac{Z}{R_0} \\ 0 & \frac{Z}{R_0} & 1 + \frac{Y}{R_0} \end{bmatrix}, & [\mathbf{R}] &\simeq \begin{bmatrix} 1 & -\frac{X}{r} & 0 \\ \frac{X}{r} & 1 & -\frac{Z}{R_0} \\ 0 & \frac{Z}{R_0} & 1 \end{bmatrix}, \\ [\mathbf{U}] &\simeq \begin{bmatrix} 1 - \frac{Y}{r} & 0 & 0 \\ 0 & 1 - \frac{Y}{r} & 0 \\ 0 & 0 & 1 + \frac{Y}{R_0} \end{bmatrix}. \end{aligned} \quad (50)$$

Ignoring the infinitesimal terms of higher order than r^{-1} and R_0^{-1} , it is immediate to check that the tensors (50) satisfy the polar decomposition $\mathbf{F} = \mathbf{R}\mathbf{U}$.

Being $\mathbf{F} = \mathbf{I} + \mathbf{H}$, it is evident from (50)₁ that the linearized displacement gradient \mathbf{H} is

$$[\mathbf{H}] \simeq \begin{bmatrix} -\frac{Y}{r} & -\frac{X}{r} & 0 \\ \frac{X}{r} & -\frac{Y}{r} & -\frac{Z}{R_0} \\ 0 & \frac{Z}{R_0} & \frac{Y}{R_0} \end{bmatrix}. \quad (51)$$

It should be noted that the displacement gradient \mathbf{H} just obtained from the linearized \mathbf{F} coincides with that calculated directly from the infinitesimal displacement field (46).

By applying the theorem of additive decomposition to the linearized displacement gradient \mathbf{H} , the skew-symmetric tensor of infinitesimal rigid rotation

620 **W** and the symmetric tensor of infinitesimal strain **E** are obtained¹³

$$[\mathbf{W}] = \frac{1}{2}[(\mathbf{H} - \mathbf{H}^T)] = \begin{bmatrix} 0 & -\omega_z & \omega_y \\ \omega_z & 0 & -\omega_x \\ -\omega_y & \omega_x & 0 \end{bmatrix} \simeq \begin{bmatrix} 0 & -\frac{X}{r} & 0 \\ \frac{X}{r} & 0 & -\frac{Z}{R_0} \\ 0 & \frac{Z}{R_0} & 0 \end{bmatrix}, \quad (52)$$

$$[\mathbf{E}] = \frac{1}{2}[(\mathbf{H} + \mathbf{H}^T)] = \begin{bmatrix} \varepsilon_x & \frac{1}{2}\gamma_{xy} & \frac{1}{2}\gamma_{xz} \\ \frac{1}{2}\gamma_{xy} & \varepsilon_y & \frac{1}{2}\gamma_{yz} \\ \frac{1}{2}\gamma_{xz} & \frac{1}{2}\gamma_{yz} & \varepsilon_z \end{bmatrix} \simeq \begin{bmatrix} -\frac{Y}{r} & 0 & 0 \\ 0 & -\frac{Y}{r} & 0 \\ 0 & 0 & \frac{Y}{R_0} \end{bmatrix}. \quad (53)$$

Among components of the tensor **W**, the rotation α around the X axis and β
622 around the Z axis are recognizable. The linearized strain state is triaxial and
principal, it depends (linearly) only on the variable Y and vanishes for $Y = 0$.

624 In the infinitesimal kinematics, the height H , the area A and the volume V
of a beam in its deformed configuration remain unchanged. This result can be
626 attained by the direct computation of variations ΔH , ΔA and ΔV , using the
strain components (53)

$$\begin{aligned} \Delta H &= \int_{-\frac{H}{2}}^{\frac{H}{2}} \varepsilon_y dY = -\frac{1}{r} \int_{-\frac{H}{2}}^{\frac{H}{2}} Y dY = 0, \\ \Delta A &= \int_A (\varepsilon_x + \varepsilon_y) dA = -\frac{2B}{r} \int_{-\frac{H}{2}}^{\frac{H}{2}} Y dY = 0, \\ \Delta V &= \int_V (\varepsilon_x + \varepsilon_y + \varepsilon_z) dV = -\frac{LB}{R_0} \int_{-\frac{H}{2}}^{\frac{H}{2}} Y dY = 0. \end{aligned} \quad (54)$$

628 Alternatively, the linearization of (33), (34) and (36) yield: $H' = H$, $A' = BH$
and $V' = BHL$, respectively¹⁴. With the linearization, the Piola-Kirchhoff stress
630 tensor (15) becomes

$$[\mathbf{T}_R] = \begin{bmatrix} S \cos \frac{X}{r} & -S \sin \frac{X}{r} & 0 \\ S \sin \frac{X}{r} \cos \frac{Z}{R_0} & S \cos \frac{X}{r} \cos \frac{Z}{R_0} & -S_Z \sin \frac{Z}{R_0} \\ S \sin \frac{X}{r} \sin \frac{Z}{R_0} & S \cos \frac{X}{r} \sin \frac{Z}{R_0} & S_Z \cos \frac{Z}{R_0} \end{bmatrix} \simeq \begin{bmatrix} S & 0 & 0 \\ 0 & S & 0 \\ 0 & 0 & S_Z \end{bmatrix}, \quad (55)$$

¹³After linearization, the following relationships hold: $\mathbf{R} = \mathbf{I} + \mathbf{W}$, $\mathbf{U} = \mathbf{I} + \mathbf{E}$.

¹⁴Using the Taylor series expansions, the following approximation is employed:

$$\sinh \frac{H}{2r} \simeq \frac{H}{2r} + o(r^{-2}),$$

as well as similar expressions for different arguments of hyperbolic sine function.

where ¹⁵

$$\begin{aligned} S &= 2\lambda [a + b(\lambda^2 + \lambda_Z^2) + c\lambda^2\lambda_Z^2] - \frac{d}{\lambda} \simeq 4Y \left[-\frac{a + 3b + 2c}{r} + \frac{b + c}{R_0} \right], \\ S_Z &= 2\lambda_Z[a + 2b\lambda^2 + c\lambda^4] - \frac{d}{\lambda_Z} \simeq -4Y \left[\frac{2(b + c)}{r} + \frac{a + 2b + c}{R_0} \right]. \end{aligned} \quad (56)$$

The linearized Piola-Kirchhoff stress state is triaxial and principal, it depends (linearly) only on the variable Y and vanishes for $Y = 0$. The linearization of the Cauchy stress components (41) gives ¹⁶

$$\begin{aligned} T_1 &= T_2 \simeq 4Y \left(-\frac{a + 3b + 2c}{r} + \frac{b + c}{R_0} \right), \\ T_3 &\simeq 4Y \left[-\frac{2(b + c)}{r} + \frac{a + 2b + c}{R_0} \right], \end{aligned} \quad (57)$$

showing how these stress components are equal to components (56). In fact, as is well known, in the infinitesimal theory the Piola-Kirchhoff and Cauchy stress measures coincide. Moreover, the neutral axis of strain coincides with that of the stress and pass through the centroid of the cross section.

The linearization of the four expressions, obtained from the calculus of integrals (44), provides

$$\begin{aligned} 2a \left(1 + \frac{r}{R_0} \right) BH - 8a \frac{r^3}{R_0} \sinh \left(\frac{H}{2r} \right) \sin \left(\frac{B}{2r} \right) &\simeq 2a BH, \\ 4b \left(1 + \frac{r}{R_0} \right) rB \sinh \left(\frac{H}{r} \right) - \frac{16}{3} b \frac{r^3}{R_0} \sinh \left(\frac{3H}{2r} \right) \sin \left(\frac{B}{2r} \right) &\simeq 4b BH, \\ c \left(1 + \frac{r}{R_0} \right) rB \sinh \left(\frac{2H}{r} \right) - \frac{8}{5} c \frac{r^3}{R_0} \sinh \left(\frac{5H}{2r} \right) \sin \left(\frac{B}{2r} \right) &\simeq 2c BH, \\ - (2a + 4b + 2c) \frac{rR_0}{r + R_0} \left\{ \frac{BH}{r} - B \ln \left[\frac{r + R_0 - r e^{\frac{H}{2r}}}{r + R_0 - r e^{-\frac{H}{2r}}} \right] \right. & \\ \left. + \frac{(r + R_0) B^3 \sinh \left(\frac{H}{2r} \right)}{12r [2r(r + R_0) \cosh \left(\frac{H}{2r} \right) - (2r^2 + 2rR_0 + R_0^2)]} \right\} &\simeq -(2a + 4b + 2c) BH. \end{aligned} \quad (58)$$

¹⁵Using the Taylor series expansions, the following approximation is employed:

$$\frac{1}{\lambda} \simeq 1 + \frac{Y}{r} + o(r^{-1}),$$

and the relationship among the constitutive constants (9) has been used to obtain ((56).

¹⁶Using the Taylor series expansions, the following approximation is employed:

$$\frac{1}{\lambda^2 \lambda_Z} \simeq 1 + \frac{2Y}{r} - \frac{Y}{R_0} + o(r^{-1}) + o(R_0^{-1}).$$

The sum of these four terms shows that the normal force n in the linearized
 642 theory is null.

The linearization of the four expressions, obtained from the calculus of inte-
 644 grals (45), provides

$$\begin{aligned}
 & 2a \left(1 + \frac{r}{R_0}\right) rBH - 8a \left(1 + \frac{2r}{R_0}\right) r^3 \sinh\left(\frac{H}{2r}\right) \sin\left(\frac{B}{2r}\right) \\
 & + a \frac{r^4}{R_0} \sinh\left(\frac{H}{r}\right) \left[\sin\left(\frac{B}{r}\right) + \frac{B}{r}\right] \simeq \frac{a}{12pR_0} [(2p-1)BH^3 + B^3H], \\
 & 4b \left(1 + \frac{r}{R_0}\right) r^2B \sinh\left(\frac{H}{r}\right) - \frac{16}{3}b \left(1 + \frac{2r}{R_0}\right) r^3 \sinh\left(\frac{3H}{2r}\right) \sin\left(\frac{B}{2r}\right) + \\
 & b \frac{r^4}{R_0} \sinh\left(\frac{2H}{r}\right) \left[\sin\left(\frac{B}{r}\right) + \frac{B}{r}\right] \simeq \frac{2b}{12pR_0} ([2p-5]BH^3 + B^3H), \\
 & c \left(1 + \frac{r}{R_0}\right) r^2B \sinh\left(\frac{2H}{r}\right) - \frac{8}{5}c \left(1 + \frac{2r}{R_0}\right) r^3 \sinh\left(\frac{5H}{2r}\right) \sin\left(\frac{B}{2r}\right) + \\
 & \frac{c}{3} \frac{r^4}{R_0} \sinh\left(\frac{3H}{r}\right) \left[\sin\left(\frac{B}{r}\right) + \frac{B}{r}\right] \simeq \frac{c}{12pR_0} ([2p-9]BH^3 + B^3H), \\
 & - (2a + 4b + 2c) \left\{ \frac{rR_0B}{r+R_0} \left[H - R_0 \ln \left(\frac{r+R_0 - r e^{-\frac{H}{2r}}}{r+R_0 - r e^{\frac{H}{2r}}} \right) \right] \right. \\
 & \quad \left. - \frac{R_0^2 B^3 \left(e^{\frac{H}{r}} - 1 \right)}{24 \left[\left(e^{\frac{H}{2r}} - 1 \right) r - R_0 \right] \left[\left(e^{\frac{H}{2r}} - 1 \right) r + R_0 e^{\frac{H}{2r}} \right]} \right\} \\
 & \simeq \frac{a+2b+c}{12pR_0} ([2p+1]BH^3 - B^3H),
 \end{aligned} \tag{59}$$

where, using (23) with $p = \frac{a+3b+2c}{b+c}$, the radius r has been replaced with the
 646 radius R_0 . The sum of these four terms gives the linearized moment-curvature
 relationships

$$m_x = \frac{4(a+b)(a+4b+3c)}{a+3b+2c} \frac{BH^3}{12} \frac{1}{R_0}. \tag{60}$$

It is important to note that the linearized stresses (56), or equivalently the
 (57), differ from the corresponding stress components of linear theory. This is
 650 obviously due to the different constitutive laws adopted in the two theories: the
 compressible Mooney-Rivlin law in nonlinear theory and the Navier inverse law
 652 in linear theory

$$\bar{\mathbf{T}} = 2G \mathbf{E} + \bar{\lambda}(tr \mathbf{E}) \mathbf{I}, \tag{61}$$

where G and $\bar{\lambda}$ are the Lamé constants and $tr \mathbf{E} = \varepsilon_x + \varepsilon_y + \varepsilon_z$. The diagonal
 654 components of $\bar{\mathbf{T}}$ are denoted by $\sigma_x, \sigma_y, \sigma_z$. However, certain conditions can be

established for the constitutive parameters a , b and c of a compressible Mooney-
656 Rivlin material in order to reproduce the same stresses of the classical linear
theory. Equating the component $\sigma_x = 2G \epsilon_x + \bar{\lambda}(\epsilon_x + \epsilon_y + \epsilon_z)$ of (61) with the
658 linearized expression (56)₁ of S , with $-\frac{Y}{r} = \epsilon_x = \epsilon_y$ and $\frac{Y}{R_0} = \epsilon_z$ according to
(53), the following relations are obtained:

$$\begin{cases} G = 2(a + b) \\ \bar{\lambda} = 4(b + c) \end{cases}. \quad (62)$$

660 The Lamé constants G and $\bar{\lambda}$ can be then converted into the pair of elastic
constants E and ν

$$\begin{cases} E = \frac{G(3\bar{\lambda} + 2G)}{\bar{\lambda} + G} = \frac{4(a + b)(a + 4b + 3c)}{a + 3b + 2c} \\ \nu = \frac{\bar{\lambda}}{2(\bar{\lambda} + G)} = \frac{b + c}{a + 3b + 2c} \end{cases}. \quad (63)$$

662 Introducing the strain tensor \mathbf{E} , in the form specified by (53), into the consti-
tutive law (61), remembering that $R_0 = \nu r$ and using relations (63), the stress
664 tensor $\bar{\mathbf{T}}$ assumes the following form:

$$[\bar{\mathbf{T}}] = \begin{bmatrix} 0 & 0 & 0 \\ 0 & 0 & 0 \\ 0 & 0 & E \epsilon_z \end{bmatrix}, \quad (64)$$

showing, as is well known, that in the linearized theory the stress state is uniaxial
666 being different from zero only the component σ_z ¹⁷.

Finally, it can be observed that, replacing (63)₂ into (23), the relationship
668 (47)₂ is recovered. Moreover, being $J_X = \frac{BH^3}{12}$, the substitution of (63)₁ into
(60) provides the linear moment-curvature relation (47)₁.

¹⁷Of course, the same result can be achieved for a compressible Mooney-Rivlin material
that satisfies the conditions (62). In effect, replacing (63) into (56), it is found

$$\begin{aligned} S &= \left[-(a + 3b + 2c) + \frac{b + c}{\nu} \right] \frac{4Y}{r} = 0, \\ S_Z &= [-2(b + c)\nu + (a + 2b + c)] \frac{4Y}{R_0} = E \epsilon_z. \end{aligned}$$

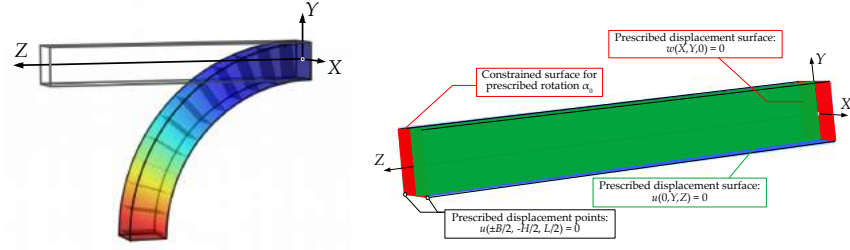
670 With these last observations, the linearization procedure which leads from
the finite to the infinitesimal bending of a beam is completed.

672 3. The numerical and experimental analyses

3.1. Numerical analysis

674 By using a free software based on the finite element method (FEM), nu-
merical simulations have been carried out. The approach is aimed to model
676 numerically the flexion of the reference beam under large deformations and dis-
placements.

678 In order to reduce the computational effort, only one half beam has been
considered (*cf.* Figure 20(a)). Two different types of restraints have been used



(a) Numerical model. Deformed configuration for $\alpha_0 = \pi/2$.
(b) FE mesh. Assignment of the constraints.

Figure 20: Details about the FE model.

680 to impart proper conditions at the ends of the system. In particular, owing to
symmetry condition, the displacement component $w(X, Y, 0)$ in the XY plane
682 has been restrained at the middle cross section, making it free to exhibit the
transversal inflexion which characterizes the anticlastic effect. Furthermore,
684 the ZY middle longitudinal section of the specimen has been restrained in
terms of the displacement component $u(0, Y, Z)$. Finally, the rigid body mo-
686 tion is avoided simply by pinning the lower nodes of the middle cross section at
($\pm B/2, -H/2, 0$), thus preventing their vertical displacement component v (*cf.*

688 Figure 20(b)). Also the mesh of the FE model, composed of brick finite elements,
 realized with 40,423 linear tetrahedra at 4 nodes, is shown in Figure 20(b)).

690 By using a specific kinematic constraint the prescribed rotation α_0 , around
 an axis parallel to the X axis, has been imposed at the edge surface $Z = L/2$.
 692 As a result, the plane surface of the beam end behaves as if it was glued to an
 undeformable rigid body¹⁸.

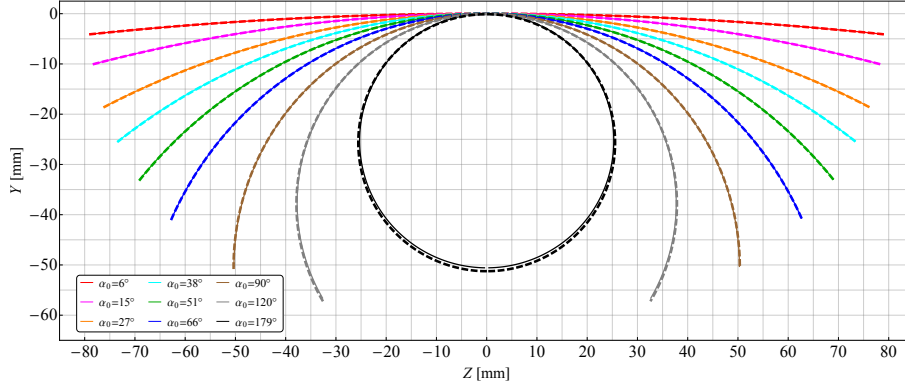
694 It should be remarked that the presence of a kinematic constraint produces
 an unwanted effect as it imparts an unnatural rigid behaviour to the end cross
 696 section, thus inhibiting its deformation in its own plane. Therefore, no anti-
 clastic effect can be observed in the end cross section, and this disturbance is
 698 expected to affect a certain terminal portion of the beam¹⁹.

The stored energy function for a compressible Mooney-Rivlin material with
 700 the constitutive constants corresponding to a Neoprene filled rubber (*cf.* Section
 2.2 of [32]), has been introduced in the FE code.

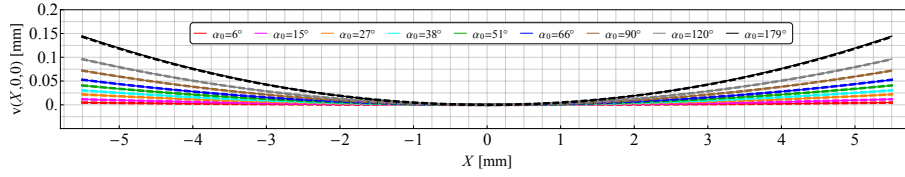
702 Figure 21(a) shows the deformed configuration of the basic line of the refer-
 ence beam ($X = Y = 0$ and $Z = Z$) varying the angle α_0 . Solid lines display
 704 the results given by the theoretical model of Section 2.4, whereas results pro-
 vided by the FE model are reported with dashed lines. A good agreement is
 706 shown between the numerical and analytical results, with special reference to
 he central part of the basic line. The discrepancy increases going toward the
 708 beam ends, and it grows as the angle α_0 increases. A similar trend occurs
 also for the vertical displacements $v(X, 0, 0)$ with respect to the traversal line

¹⁸This rigid constraint allows reproducing the experimental set-up, described in Section 3.2,
 where the ends of the beam are glued to the metallic plates of the mechanical apparatus.

¹⁹The imparting the flexure angle $2\alpha_0$ to the beam ends with the FE approach deserves
 some difficulties. To this aim, a distribution of stress should be applied at the two end cross
 sections in order to reproduce a constant bending moment along the longitudinal axis of the
 beam. As an alternative, a displacement field could be imposed at the end cross sections.
 Based on the assumption of planarity of the cross sections, this should produce a deformed
 configuration resembling that a circumferential arc. However, in both situations, stresses and
 displacements to be applied depend on the solution of the equilibrium problem and they are
 not known *a priori*.



(a) Deformed configuration of the longitudinal centroid line ($X = 0$, $Y = 0$, Z).



(b) Displacement component $v(0, 0, Z)$ of the transversal centroid line ($X Y = 0$, $Z = 0$).

Figure 21: Comparison between the results provided by the numerical (dashed lines) and theoretical (solid lines) models.

710 $X = X$, $Y = Z = 0$ (cf. Figure 21(b)). To assess the gap between the values
provided by the theoretical model and those obtained by the numerical analysis,
712 the relative error $\epsilon_{r,d}$ for displacements is introduced, being $\epsilon_{r,d} = \epsilon/v_{TM} 100$,
 $\epsilon = v_{TM} - v_{FEM}$ (absolute error), v_{TM} is the value furnished by the theoretical
714 model and v_{FEM} that obtained by the FE analysis. Figure 22 shows the max-
imum errors varying α_0 . In particular, for $\alpha_0 = 179^\circ$, at the ends of the beam
716 ($Z = \pm L/2$), the relative error $\epsilon_{r,d}$ reaches the maximum value of about 1.39%.
Concerning the transversal displacement field reported in Figure 21(b) (strictly
718 connected to the anticlastic effect), for $\alpha_0 = 179^\circ$, $\epsilon_{r,d}$ reaches the maximum
value of about 0.92% at the beam lateral surface, namely at $X = \pm B/2$, (cf.
720 Figure 22).

For the limit case with $\alpha_0 = 179^\circ$, that is for a beam deformed like a ring,
722 Figure 23 shows the stretches λ_Z for each point of the middle cross section

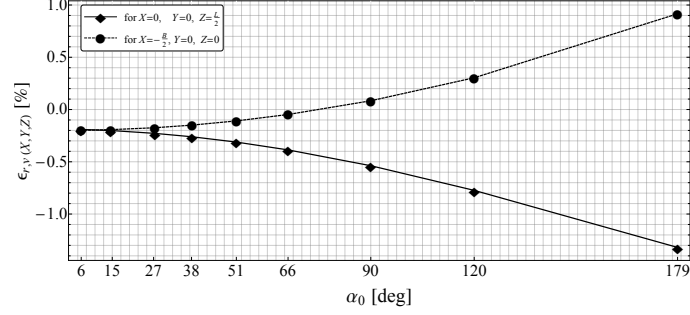


Figure 22: Relative error affecting the vertical displacements varying the angle α_0 . Vertical displacements $v(0, 0, L/2)$ (solid line) and $v(-B/2, 0, 0)$ (dashed line).

($Z = 0$), evaluated both in the reference and spatial configurations (*cf.* Figures 23(a) and 23(b)). Dashed iso-lines in the contour plot denote the results

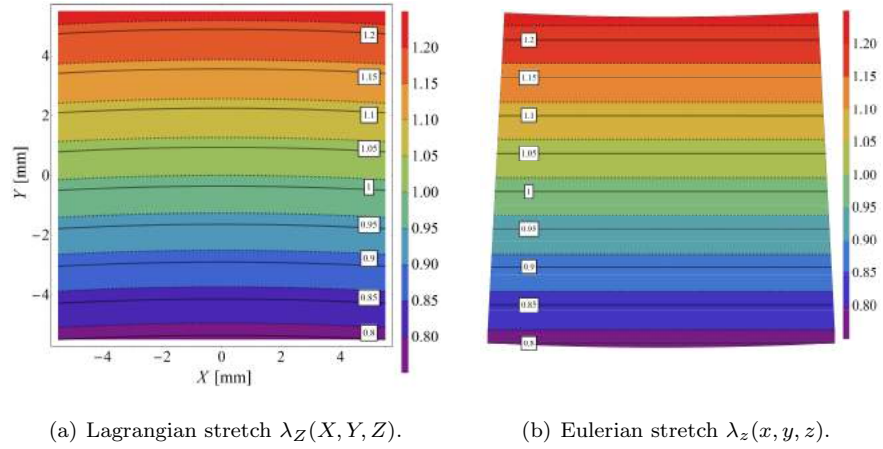


Figure 23: Numerical (solid iso-lines with framed value) and theoretical (contour-plot with dotted iso-lines) results for both the reference and deformed configurations.

724

provided by the theoretical model, whereas FE results are overlapped through
 726 black thick iso-lines with the addition of their value. As shown, the discrepancy
 between the two approaches in terms of the longitudinal stretches are very small
 728 for both Lagrangian and Eulerian descriptions. Such differences are shown in
 Figure 24, where the relative error $\epsilon_{r,\lambda}$ for stretches in the Eulerian description

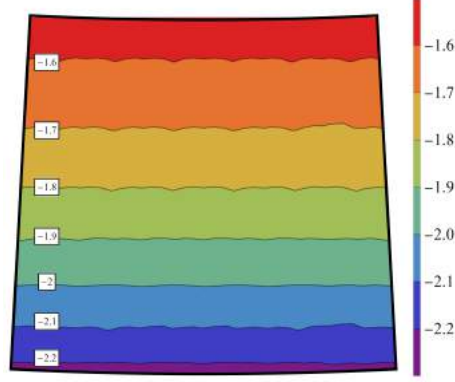


Figure 24: Relative errors (experimental with respect to the theoretical) about the Eulerian stretch $\lambda_z(x, y, z)$.

are displayed²⁰. The major gap occurs at the bottom edge, where the FE analysis slightly overestimates the results of the theoretical model by a few percentage points.

Figure 25 shows the comparisons in terms of longitudinal stresses. In particular, Figure 25(a) highlights the Piola-Kirchhoff stress component $T_{R,33}$, whereas the Cauchy stress component T_{33} is plotted in Figure 25(b). The comparison shows slight differences between the results obtained with the two approaches. The absolute errors concerning the Cauchy stress component ($\epsilon = T_{33,TM} - T_{33,FEM}$) are shown in Figure 26²¹.

3.2. Experimental analysis

An experimental analysis for the bending of the reference beam is carried out in this Section and the obtained results are compared with those provided by the theoretical model. Recently, a proper mechanical prototype (see Figure 28) has been designed and manufactured for this type of experimental investigation

²⁰Oscillations in the iso-lines are due to the fact that the numerical results have been assessed at the Gauss nodes of the FE mesh.

²¹Note that the relative errors for stresses become meaningless in the central area of the cross section as the stresses vanish there.

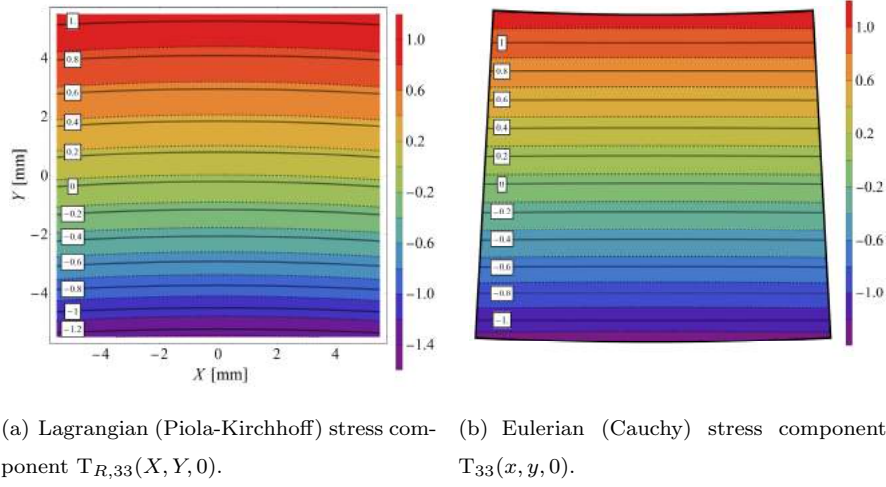


Figure 25: FE (solid iso-lines with framed value) and theoretical (contour-plot with dotted iso-lines) results for both the reference and deformed configurations of the beam cross section at $Z = 0$.

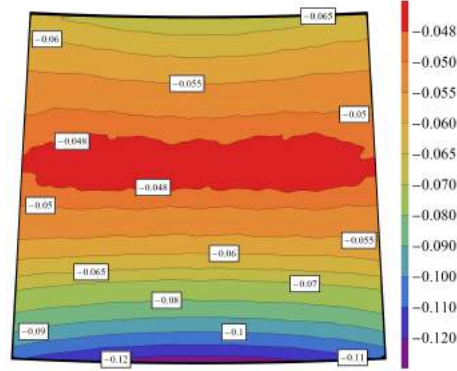


Figure 26: Absolute error (experimental with respect to the theoretical) of the Cauchy stress component $T_{33}(x, y, 0)$.

744 [30]. Concerning the realization of this test equipment, the main difficulty is to
 reproduce a pure bending state avoiding unwanted effects, as the occurrence of
 746 axial or shear forces. The proposed mechanical apparatus induces bending by
 imposing the prescribed rotations at the ends of the sample, but letting it free

748 to exhibit its elastic retaining force²².

750 The large bending of the sample is achieved by two pantographs. The two
pairs of arms of each pantograph are constrained, in a bilateral manner, to slide
on two horizontal guides. These guides are connected by a threaded vertical
752 bar, fixed to the lower guide. The rotation of the activation handle generates
a vertical motion of the lower guide approaching (or moving away from) the
upper one. The mutual vertical translation of the horizontal guides actuates
754 the scissor devices which imparts a rotation to the slanted arms around their
fulcrum. The slanted arms of each pantograph are connected by five hinges and
756 they rotate at each turn of the activation knob. A rigid block is fixed to the
upper internal hinge. A little plate with a L-shaped profile is constrained on this
758 block. The end of the sample is glued to the plate. Knowing the thread pitch of
the manual actuation device, it is possible to assess exactly the rotation angle α_0
760 imparted at the ends of the specimen. The nonlinear correspondence between
the number of revolutions of the manual actuation device and the angle α_0 has
762 been accurately estimated. The number of rotations of the activation handle
necessary to produce some values of the angle α_0 are reported in Figure 27. Such
764 values have been assessed through a numerical algorithm and, experimentally,
by measuring the rotation of the rigid block with the digital image correlation
766 (DIC) apparatus.

768 A DIC instrumentation, a full-field image analysis method based on grey
value digital images optical monitoring, has been used to acquire the experi-
770 mental data, with specific reference to the displacement field. In particular,
Istra Q-400 instrumentation of the Dantec Dynamic s.b.m., with its own inter-
772 nal hardware and software equipments, has been used. The calibration of the
optical system ensures a monitoring resolution of $\pm 10 \mu m$. By setting the ac-
774 quisition procedure in stereo-mode, the entire three-dimensional displacement

²²It should be remarked that the inevitable frictions of the mechanisms during the experi-
mental tests run against to the elastic retaining force. This leads to an overestimation of the
stiffness of the tested sample.

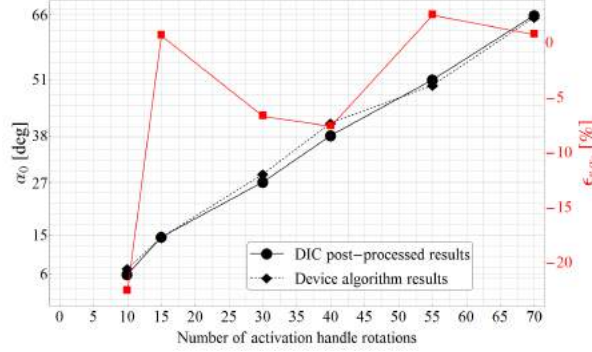
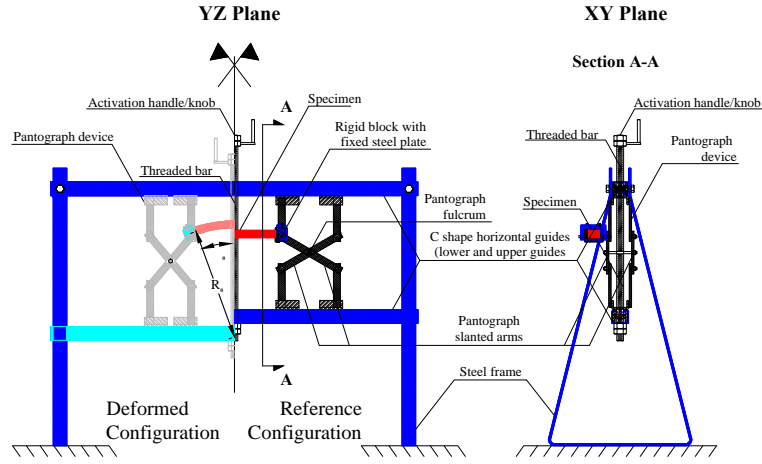


Figure 27: Rotation angle α_0 monitored with DIC (solid line) and calculated analytically (dashed line) varying the activation handle of the mechanical device.

field of the external surface of the specimen can be assessed. Two different acquisition layouts have been performed: The first set-up, named in the following *upper view*, consists in the acquisition over the upper-surface of the specimen, that is the horizontal plane $Y = H/2$; the second acquisition set-up, named *lateral view*, consists in the lateral monitoring of the specimen on the vertical plane $X = B/2$. Some details of the upper and lateral views are shown in Figure 29(a). During the bending test, only the two above mentioned surfaces of the specimen are monitored. Some reference lines inside the two monitored surfaces of the sample, along which the line plots are made, are identified as shown in Figure 29(b). Obviously, physical fields inside the beam cannot be measured through the DIC.

The vertical displacements $v(B/2, 0, Z)$ of the reference line L_h varying the angle α_0 are shown in Figure 30. The results provided by the experimental analysis are represented with dashed lines, whereas the solid lines denote the results given by the theoretical model. The experimental data and the theoretical predictions are close, showing that the two approaches provide similar results. Note that in the central part of the basic line the two approaches provide almost the same results. For $\alpha_0 > 66^\circ$, the specimen is no longer able to develop an effective retaining force, thus the experimental results with $\alpha_0 > 66^\circ$ appear less accurate. Note also that in the range of α_0 here investigated, the



(a) Mechanical schedule.



(b) Frontal view.



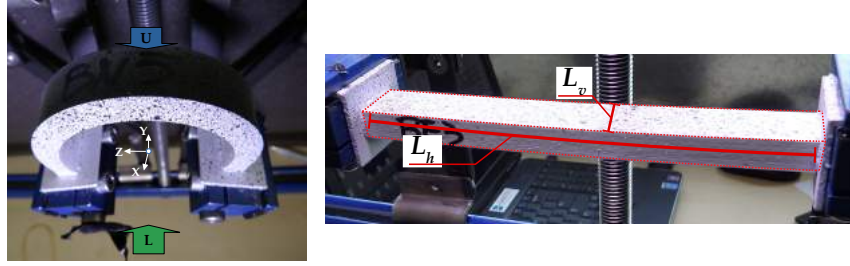
(c) Lateral view.

Figure 28: Mechanical equipment for large bending test.

maximum errors occur at the end cross sections ($Z = \pm L/2$).

796 Figure 31 shows the maximum values of the gap between the two solutions.
 798 For low values of the angle α_0 , significant errors occur owing to the initial
 frictions of the test machine, that overcome the retaining force of the sample.
 798 The iso-lines provided by the experimental tests (solid lines) are close to those
 800 obtained from the theoretical prediction.

The deformed configurations assumed by the specimen during the experi-
 802 mental tests are shown in Figure 33 for the first six values assumed by α_0 . The



(a) Monitored specimen under bending: Lateral (L) and upper (U) views. (b) Experimental reference line on the monitored specimen: L_v vertical line for the upper monitoring and L_h horizontal line for the lateral monitoring.

Figure 29: DIC monitoring views and reference lines.

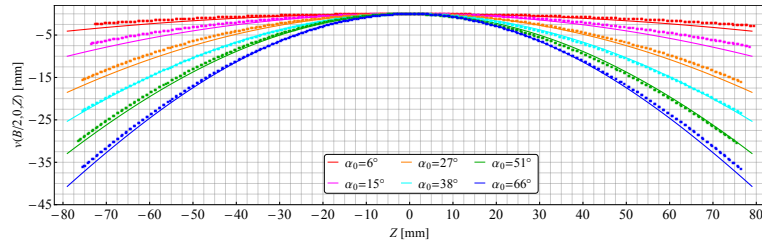


Figure 30: Vertical displacements component $v(B/2, 0, Z)$ along the reference line L_h varying the angle α_0 : Experimental results (dashed lines) and theoretical prediction (solid lines).

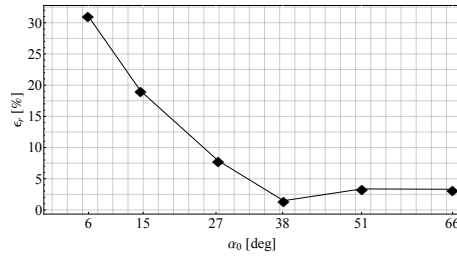
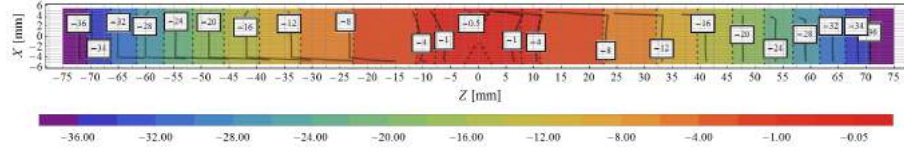
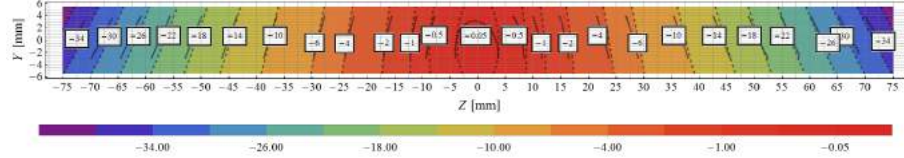


Figure 31: Relative error about the vertical displacements $v(B/2, 0, 0)$ (experimental with respect to the theoretical) varying the angle α_0 .

804 same figure highlights the contour-plots of the rotation field measured on the lateral surface of the sample. As expected from the hypothesis of conservation of the planarity of the cross sections, the iso-lines represented in the reference



(a) Displacement component $v(X, H/2, Z)$ at the upper specimen surface.



(b) Displacement component $v(B/2, Y, Z)$ at the lateral specimen surface.

Figure 32: Experimental (solid iso-lines with framed value) and theoretical (contour-plot with dotted iso-lines) results.

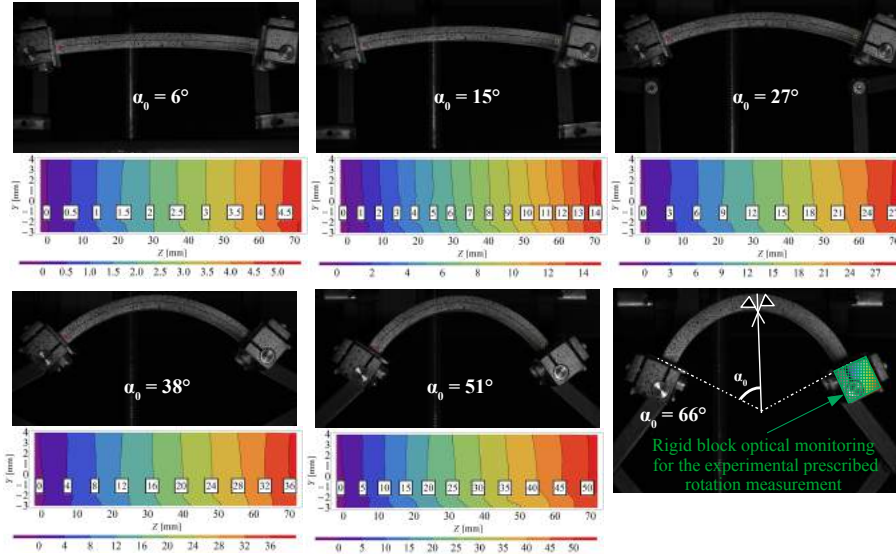


Figure 33: Contour-plot of the rotation field around the X axis in the reference configuration. Acquired DIC data for some values of the angle α_0 .

806 configuration are equispaced and sufficiently straight²³.

²³The last image of Figure 33 shows the rigid block that, monitored with the DIC instrument, allows obtaining the rotations shown in Figure 27.

3.3. Discussion

808 The vertical displacements $v(B/2, 0, Z)$ obtained from the theoretical model, numerical simulations and experimental investigation are compared in Figure 34. As reported in Section 3.2, the experimental results referred to imparted rota-

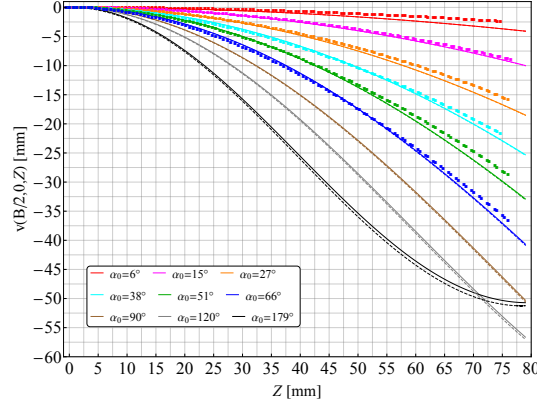
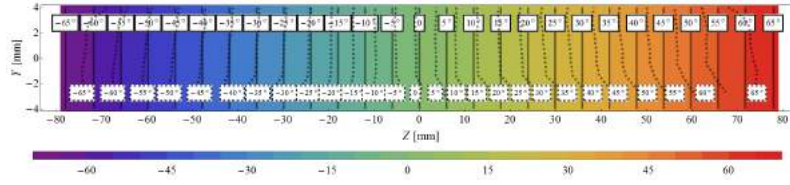


Figure 34: Displacements component $v(B/2, 0, Z)$. Theoretical model (solid lines), numerical analysis (dashed lines) and experimental analysis (cross marker) for $Z \in [0, L/2]$ varying α_0 .

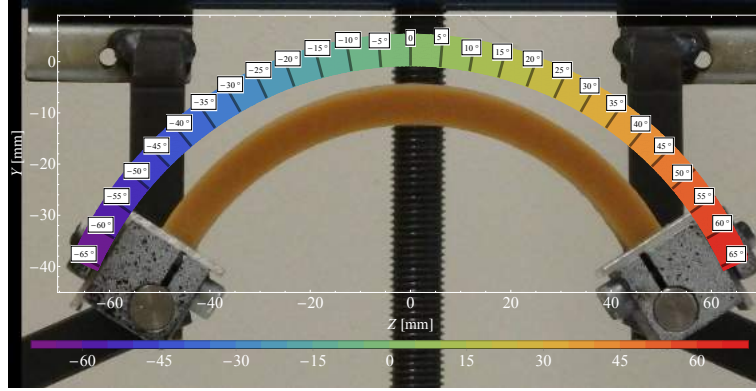
810 tions $\alpha_0 \leq 66^\circ$ owing to technical difficulties encountered during the tests. Note that the shape of the curve relative to the case $\alpha_0 = 179^\circ$ is different from the others, since the ends of the beam are also pushed upwards to form the ring (*cf.* Figure 21(a)). As shown, for the selected values of α_0 , the curves are very close to each other.

816 With more detail, the rotations for the last case of Figure 33 corresponding to $\alpha_0 = 66^\circ$ are illustrated in Figure 35, where the rotation iso-lines of the cross sections are also reported. The amount of rotation undergone by the beam cross sections are shown in Figure 35(a) in the reference configuration²⁴. Owing to symmetry, the middle cross section does not exhibit rotation, whereas the other cross sections highlighted in the figure correspond to the cross sections that undergo the rotations reported in the black boxes. These cross sections are perfectly equi-spaced each other. As shown, the theoretical model (contour-

²⁴For sake of representation, the height of the specimen has been doubled.



(a) Lateral surface of the specimen in the Lagrangian description.



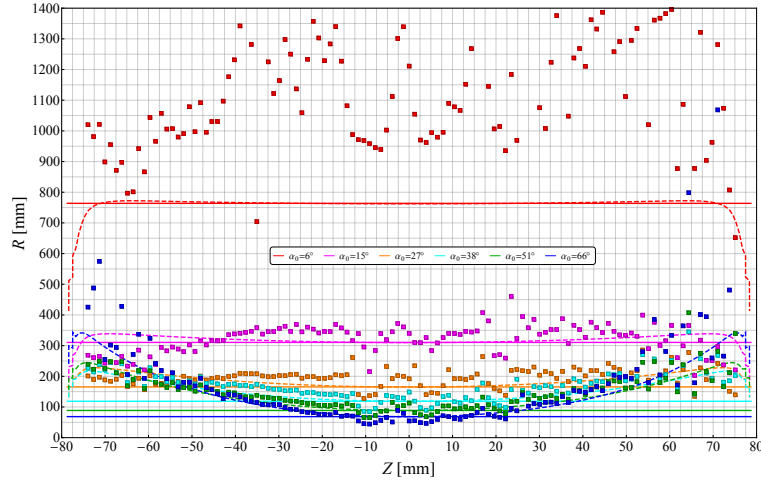
(b) Lateral surface of the specimen in the Eulerian description.

Figure 35: Comparison between the rotation field provided by the theoretical model (contour-plot), FE analysis (solid lines) and the experimental analysis (dashed iso-lines, for the reference configuration only) for $\alpha_0 = 66^\circ$.

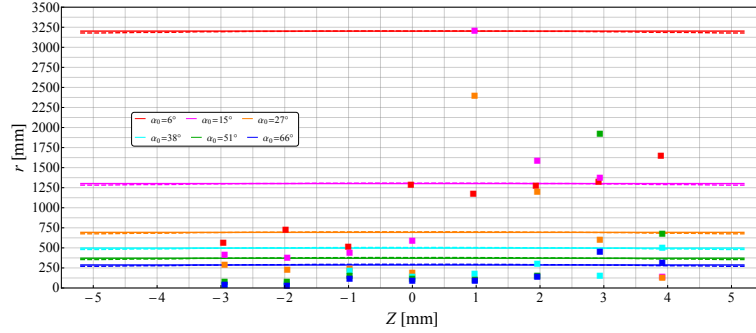
824 plot) and the FE analysis (continuous iso-lines) provide coincident results, while
the results obtained by the experimental analysis (dashed lines) differ a little.
826 Making reference to the Eulerian description, Figure 35(b) shows the same ro-
tations in the deformed configuration. In such figure some technical difficulties
828 were encountered in representing the experimental results, which came out of
the profile of the deformed specimen. For this reason, only the results of the
830 theoretical model and those of the FE analysis are compared, which substan-
tially coincide. Note that in Figure 35(b) the vertical traces of the cross sections,
832 positioned on the lateral surface of the specimen, remain rectilinear after the
deformation. This confirms the hypothesis of conservation of the planarity of
834 the beam cross sections.

Figure 36(a) shows the longitudinal radius R evaluated along the reference

line L_h for $\alpha_0 \leq 66^\circ$. As expected from the theoretical model, this geomet-



(a) Longitudinal radius of curvature R along the reference line L_h .



(b) Anticlastic radius of curvature r along the reference line L_v .

Figure 36: Variation of the radii of curvature along the reference lines: Theoretical model (solid lines), numerical analysis (dashed lines) and experimental analysis (dotted lines with cross marker).

836

ric parameter is constant along the beam axis. Apart the end regions of the
838 beam, the same result is provided by the FE analysis (the noise produced by
the imposition of the boundary conditions has been discussed in Section 3.1).

840 Experimental results are represented by a set of discrete points. The spread
affecting the experimental values for $\alpha_0 = 6^\circ$ is due to the initial friction of the
842 test machine. As expected, as the angle α_0 increases, the radius R decreases

and the experimental values converge to the theoretical and numerical results,
 844 showing a constant trend along the beam axis. In Figure 36(b), the results of
 the three different methods are compared in terms of the anticlastic radius r for
 846 the reference line L_v at the middle cross section. For each value of the angle α_0 ,
 the theoretical model predicts a constant transverse radius r . The FE analysis
 848 provides the same constant values along the transversal direction²⁵. Conversely,
 as discussed in Section 3.2, the results provided by the experimental analysis
 850 are not very reliable due to the difficulty of measuring displacements of small
 amount.

852 To assess in detail the transversal radius of curvature r at each point of the
 middle cross section, a specific FE analysis was carried out²⁶. The values of r
 854 for $\alpha_0 = 90^\circ$ and $\alpha_0 = 179^\circ$ are shown in Figures 37(a) and 37(b), respectively.
 It is remarked that the theoretical model assumes a single value of r for all

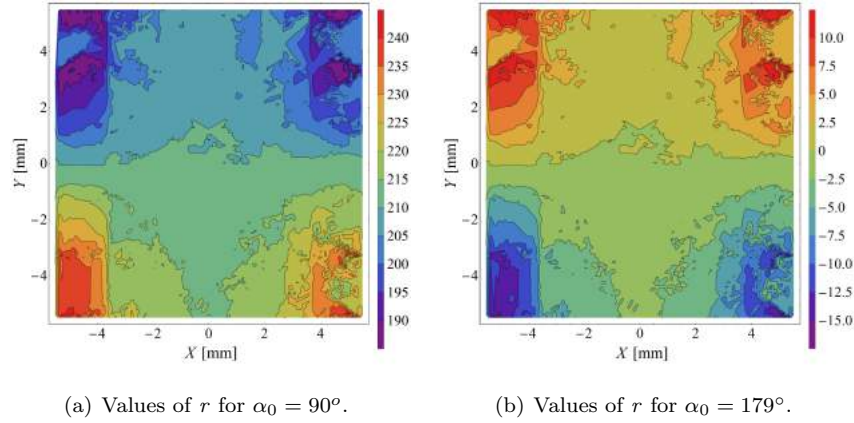


Figure 37: Transversal radius of curvature r provided by the FE analysis for each point of the middle cross section.

856 points of the transversal basic line $X = X$ and $Y = Z = 0$, coinciding with

²⁵The FE results in the middle section are not affected by the discrepancies generated by the boundary conditions.

²⁶The radius r has been evaluated locally as the radius of the osculating circle passing through three neighbouring points of the reference line in the deformed configuration.

the value of r at the centroid, r_{TM} . As it can be seen in Figure 37, such an
 858 assumption is well satisfied, also in the limit case with $\alpha_0 = 179^\circ$.

Further considerations on the trend of r within the cross section can be
 860 made from Figures 37. In particular, the radius r varies slightly inside the core
 of the cross section, assuming locally values close to r_{TM} . Instead, significant
 862 differences occur in the correspondence of the four vertices of the cross section.
 This is due to the fact that vertices are far from the transversal basic line.
 864 Moreover, the material fibres are less confined in the neighbouring of vertices,
 thus keeping a certain capacity to deform. The edge of the beam cross sec-
 866 tion near the upper vertices tends to form curls and therefore r is lower than
 r_{TM} there. Conversely, the edge of the cross section near the lower vertices
 868 tends to become straight, and therefore in these zones r is larger than r_{TM} .
 Figure 38 shows the deformed configurations assumed by the upper and lower
 870 edges of the middle cross section for $\alpha_0 = 179^\circ$ (the amplitude of the in-plane
 displacement components $u(X, \pm H/2, 0)$ and $v(X, \pm H/2, 0)$ has been magni-
 872 fied and the deformed profiles overlapped at $X = 0$ to make the image more
 clear) together with the profile assumed by the transversal basic line, which
 assumes the radius of curvature $r = r_{TM}$. The distribution of the longitudinal

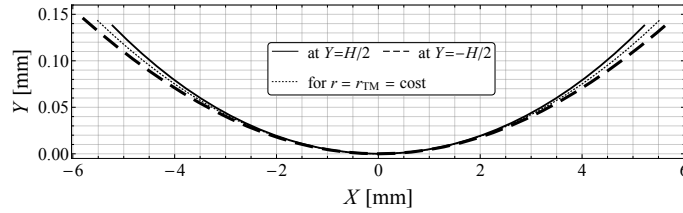
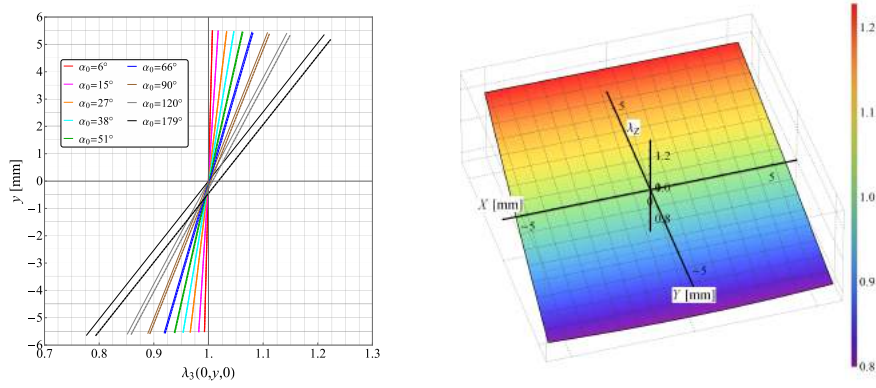


Figure 38: Deformed configuration of the upper (solid line) and lower (dashed line) edges of
 the middle cross section for $\alpha_0 = 179^\circ$ provided by the FE analysis.

874

stretches $\lambda_z(0, y, 0)$ in the Eulerian configuration varying α_0 are shown in Fig-
 876 ure 39(a). Based on the theoretical prediction, the longitudinal stretches exhibit
 a linear variation along the y axis, assuming unitary value at the origin. Such
 878 linear trend do not depend on the Eulerian variable x . Therefore, the vertical
 diagram of stretches remains unchanged moving transversely in the xy plane.



(a) Vertical diagrams of $\lambda_z(0, y, 0)$ varying α_0 . (b) 2D diagram of $\lambda_z(x, y, 0)$ for $\alpha_0 = 179^\circ$
Comparison between theoretical (solid lines) and FE (dashed lines) results.

Figure 39: Longitudinal stretches λ_z at the middle cross section.

In particular, all stretches $\lambda_z(x, 0, 0)$ evaluated along the x axis are unitary. As a consequence, x axis coincides with the neutral axis for the deformation (cf. Figure 39(b)). Such considerations about stretches are consequences of the hypothesis of conservation of the planarity of the cross sections. The results obtained by the theoretical model discussed above are substantially confirmed by the numerical ones provided by FE analysis.

4. Conclusions

In this paper, the equilibrium problem of hyperelastic slender beams under anticlastic bending has been investigated in the context of finite elasticity. The main difficulties in addressing this issue derive from its fully nonlinear framework, where no assumption of smallness of the deformation and displacement fields is formulated.

In [1] the displacement field of an inflexed solid has been defined by a kinematical model based on the following three assumptions: the solid is inflexed longitudinally with constant curvature; after deformation, cross sections maintain their planarity; also cross sections are inflexed transversely with constant

896 curvature. This kinematic model has been modified in the present paper consid-
 898 ering the class of slender beams, that is of solids with the longitudinal dimension
 notably prevalent on the two transversal ones.

The displacement field has been obtained by examining the contributions due
 900 to the rigid translation, the rigid rotation and the pure deformation. Given the
 nonlinearity, these contributions have coupled expressions. For each point of the
 902 beam, the deformation gradient \mathbf{F} , the rotation tensor \mathbf{R} and the stretch tensor
 \mathbf{U} have been computed. Despite the elaborate shape of the displacement field,
 904 the stretches have simple and compact expressions in terms of exponential func-
 tions (*cf.* eqn (24)). The deformation state is triaxial and non-homogeneous.
 906 Explicit formulae have been given to determine the area of cross sections and
 the volume of the beam in the deformed configuration.

908 Studied the kinematics of inflexed slender beams, a Lagrangian analysis of
 the equilibrium problem has been developed. Determined the Piola-Kirchhoff
 910 stress tensor \mathbf{T}_R for a generic hyperelastic material, the equilibrium equations
 have been derived. These equations, which must be satisfied locally, have been
 912 expressed by a very complex system of three partial differential equations. Hav-
 ing adopted the semi-inverse approach, it is unthinkable that the above system
 914 of equilibrium equations can be correctly solved for all points of the beam. Nev-
 ertheless, a basic longitudinal line (with coordinates $X = Y = 0$ and $Z = Z$)
 916 has been recognized, where the equilibrium equations are exactly satisfied.

At this point of the formulation, the stored energy function has been speci-
 918 fied by assigning it the form of the compressible Mooney-Rivlin law. To assess
 the accuracy of the displacement field in correspondence of points different from
 920 those belonging to the basic line, by means of numerical analyses it has been
 estimated how much the equilibrium equations deviate from zero as one moves
 922 away from the basic line. By varying the geometrical and the constitutive pa-
 rameters, the existence of a central core surrounding the basic line, where the
 924 equilibrium equations are close to zero, has been highlighted. The most impor-
 tant parameter is the length of the beam L , in the sense that the equilibrium
 926 equations are very close to zero at each point of the beam as the length L grows.

A further verification of the obtained solution has been performed by calculating
928 the normal force and checking that it is practically zero.

With the purpose of evaluating stretches and stresses in the deformed con-
930 figuration, an Eulerian analysis has been conducted. The formulae allowing the
transition from Lagrangian coordinates to Eulerian coordinates have been de-
932 rived (*cf.* eqn (26)). These has then been used to determine the diagrams of
the stretches in the deformed cross sections (*cf.* Figure 14). The diagrams of
934 the stretches in the deformed configuration are linear. Also the neutral axis for
the deformation (line $\lambda_z = 1$) is rectilinear. All this according to the kinematic
936 model, which predicts that cross sections remain plane and rotate rigidly around
the neutral axis. This aspect of the problem could not been observed in terms
938 of Lagrangian coordinates. In addition, the line $\lambda_x = \lambda_y = 1$ is distinct from
the neutral axis $\lambda_z = 1$.

The Cauchy principal stresses has been evaluated (*cf.* eqn (41)) and the
effective stress distributions in the inflexed beam are shown by some diagrams
942 (*cf.* Figures 16 and 17). Knowing the stress distributions, the bending moment
in the deformed configuration has been determined (*cf.* eqn (42)), making it
944 possible to assess the value of the moment needed to produce a specific inflexion
angle α_0 . This has allowed to impose the boundary conditions statically through
946 the application on the two end faces of the beam of a pair of self-equilibrated
bending moments (*cf.* Figure 19).

By imposing the hypothesis of smallness of the displacement and strain fields,
the whole formulation exposed in the paper for the finite anticlastic bending
950 of hyperelastic slender beams has been linearized. All derived formulae have
been rewritten as power series. These series, which depend on the radii r and
952 R_0 , have been truncated by preserving the first order infinitesimals as $r \rightarrow \infty$
and $R_0 \rightarrow \infty$. Accordingly, the nonlinear displacement field (22) has been
954 linearized getting exactly the well-known displacement field of the linear theory
of inflexed beams (*cf.* eqn (48)). With the linearization of the deformation
956 gradient, infinitesimal strain and infinitesimal rigid rotations tensors have been
derived (*cf.* eqn (52) and (53)). Due to the Poisson effect, the linearized strain

state and stress state are triaxial and depend (linearly) only on the variable Y and vanish for $Y = 0$. Through linearization, it has been shown that, contrary to the finite theory, in the infinitesimal kinematics the height and the area of cross sections as well as the volume of the solid remain unchanged after deformation (*cf.* eqn (54)). The two stress measures of Piola-Kirchhoff and Cauchy in the linearized theory coincide. Therefore, linearizing the Piola-Kirchhoff tensor (15) and the Cauchy stress tensor (39), the same stress tensor has been obtained (*cf.* eqn (55), (56) and (57)).

Differently from the bending of nonlinear beams, in the infinitesimal theory the neutral axis of strain coincides with the neutral line of the stress and they pass through the centroid of the cross section.

Since different constitutive laws have been used, the stresses obtained with the linearization are not equal to the typical stresses of an inflexed beam in infinitesimal theory. Therefore, the relationships that must be met the constitutive parameters of a compressible Mooney-Rivlin material in order to reproduce the Lamé constants have been identified (*cf.* eqn (62)). Using these relationships, the linearized stress tensor coincides with that typical of the infinitesimal theory. In particular, the state of stress becomes uniaxial.

The linearization procedure has demonstrated the complete transition from the proposed solution for the fully nonlinear bending to the classical solution for the infinitesimal bending of beams.

In order to corroborate the theoretical model about the inflexion of slender beams in a fully nonlinear context, a numerical model and an experimental investigation have been developed. The main results provided by these two different approaches have been then compared with those provided by the theoretical model formulated in the Section 2.4.

The FEM model has been used to perform a numerical analysis. The beam has been partitioned using the 4 node tetrahedra elements. Difficulties have been encountered to impose the boundary conditions, which prescribe the rotations of the two end cross sections of the beam. As a consequence, the obtained results near the terminal portions of the beam has appeared less accurate.

For a neoprene filled rubber, the constitutive parameters of the compressible
990 Mooney-Rivlin stored energy function have been experimentally identified [32].
Therefore, a sample with the shape of a slender prismatic beam has been made
992 with this rubber-like material. The sample has been bent by imposing large
rotations to its end cross sections through a mechanical equipment prototype,
994 which has been properly designed and manufactured to perform the experimen-
tal analysis. In particular, the beam-like sample has been subjected to large
996 bending by using two pantographs. The DIC instrumentation has been used
to acquire experimental data. Such an equipment allows to measure and mon-
998 itor the entire displacement field of the specimen external surface with great
accuracy ($\pm 10 \mu m$).

1000 Based on three different approaches (theoretical model, numerical simulation
and experimental investigation), the following results for the nonlinear equilib-
1002 rium problem at hand have been found.

In the evaluation of the vertical displacement field (assessed on both the
1004 lateral and upper surfaces of the sample), the three different approaches have
yielded almost coincident results. The sample has been bent longitudinally with
1006 constant curvature, and the same radius of curvature has been evaluated with
the three methods varying the angle of rotation α_0 . This fact has corrobo-
1008 rated the first kinematic hypothesis formulated in the first part of this paper.
Moreover, owing to the anticlastic effect, also the cross sections have exhibited
1010 inflexion in their planes. With the exception of the experimental results found
for α_0 small, the transversal inflexion has occurred with constant curvature and
1012 almost the same radius of curvature has been provided by the three different
approaches varying α_0 . This has confirmed the third kinematic hypothesis.

1014 Since the displacement field inside the specimen cannot be measured through
the DIC system, for the internal points of the sample the results obtained from
1016 the theoretical model have been compared with those provided by the numerical
analysis only, founding good agreement. Concerning the displacements of the
1018 longitudinal and transverse basic lines, the two models have provided coincident
results, thus confirming the validity of the first and third hypotheses. Very

1020 similar results obtained with these two approaches have been found also for the
 rotation field of the cross sections, as well as for the stretches and stresses, which
 1022 have been evaluated both in the Lagrangian and in the Eulerian configurations.

The linear trend of the longitudinal stretches along the depth of the cross
 1024 section in the Eulerian configuration, evaluated through the FE code, has cor-
 roborated the second kinematic hypothesis of the theoretical model about the
 1026 preservation of the planarity of the cross sections after the deformation.

Acknowledgement

1028 Financial support from the Italian Ministry of Education, University and Re-
 search (MIUR) in the framework of the Project PRIN " *Modelling of constitutive*
 1030 *laws for traditional and innovative building materials*" (code 2017HFPKZY) is
 gratefully acknowledged.

- 1032 [1] L. Lanzoni, A. M. Tarantino, Finite anticlastic bending of hyperelastic
 solids and beams, *Journal of Elasticity* 131 (2) (2018) 137–170.
- 1034 [2] B. Seth, Finite strain in elastic problems, *Philosophical Transactions of the*
Royal Society of London. Series A, Mathematical and Physical Sciences
 1036 234 (738) (1935) 231–264.
- [3] R. Rivlin, Large elastic deformations of isotropic materials. V. the problem
 1038 of flexure, *Proceedings of the Royal Society of London. Series A. Mathe-*
matical and Physical Sciences 195 (1043) (1949) 463–473.
- 1040 [4] J. L. Ericksen, Deformations possible in every isotropic, incompressible,
 perfectly elastic body, *Zeitschrift für angewandte Mathematik und Physik*
 1042 (ZAMP) 5 (6) (1954) 466–489.
- [5] M. M. Carroll, Finite deformations of incompressible simple solids i.
 1044 isotropic solids, *The Quarterly Journal of Mechanics and Applied Mathe-*
matics 21 (2) (1968) 147–170.

- 1046 [6] C. C. Wang, Normal configurations and the nonlinear elastostatic prob-
 1048 lems of bending, torsion, expansion, and eversion for compressible bodies,
 Archive for Rational Mechanics and Analysis 114 (3) (1991) 195–236.
- [7] M. Aron, Y. Wang, On deformations with constant modified stretches de-
 1050 scribing the bending of rectangular blocks, The Quarterly Journal of Me-
 chanics and Applied Mathematics 48 (3) (1995) 375–387.
- 1052 [8] G. Saccomandi, Universal results in finite elasticity, non-linear elasticity:
 theory and applications, London Mathematical Society lecture notes 283
 1054 (2001) 97–134.
- [9] R. Shield, Bending of a beam or wide strip, The Quarterly Journal of
 1056 Mechanics and Applied Mathematics 45 (4) (1992) 567–573.
- [10] J. Blondin, Horace Lamb. Sur la flexion d’un ressort élastique plat; Phil.
 1058 Mag., 5e série, t. XXXI, p. 182-188; 1891, J. Phys. Theor. Appl. 1 (1)
 (1892) 182–188.
- 1060 [11] A. E. H. Love, A treatise on the mathematical theory of elasticity, Cam-
 bridge university press, 2013.
- 1062 [12] T. Wang, S. Lee, O. Zienkiewicz, A numerical analysis of large deflections of
 beams, International Journal of Mechanical Sciences 3 (3) (1961) 219–228.
- 1064 [13] T. Wang, Non-linear bending of beams with uniformly distributed loads,
 International Journal of Non-Linear Mechanics 4 (4) (1969) 389–395.
- 1066 [14] J. Holden, On the finite deflections of thin beams, International Journal of
 Solids and Structures 8 (8) (1972) 1051–1055.
- 1068 [15] R. Frisch-Fay, Flexible bars, Butterworths, 1962.
- [16] E. Reissner, On one-dimensional finite-strain beam theory: the plane prob-
 1070 lem, Zeitschrift für angewandte Mathematik und Physik ZAMP 23 (5)
 (1972) 795–804.

- 1072 [17] E. Reissner, On one-dimensional large-displacement finite-strain beam theory, *Studies in applied mathematics* 52 (2) (1973) 87–95.
- 1074 [18] E. Reissner, On finite deformations of space-curved beams, *Zeitschrift für angewandte Mathematik und Physik ZAMP* 32 (6) (1981) 734–744.
- 1076 [19] K. J. Bathe, S. Bolourchi, Large displacement analysis of three-dimensional beam structures, *International Journal for Numerical Methods in Engineering* 14 (7) (1979) 961–986.
- 1078 [20] J. C. Simo, A finite strain beam formulation. the three-dimensional dynamic problem. part i, *Computer methods in applied mechanics and engineering* 49 (1) (1985) 55–70.
- 1080 [21] A. Cardona, M. G  radin, A beam finite element non-linear theory with finite rotations, *International journal for numerical methods in engineering* 26 (11) (1988) 2403–2438.
- 1082 [22] J. C. Simo, L. Vu-Quoc, On the dynamics in space of rods undergoing large motions a geometrically exact approach, *Computer methods in applied mechanics and engineering* 66 (2) (1988) 125–161.
- 1086 [23] A. Ibrahimbegovi  , On finite element implementation of geometrically non-linear reissner’s beam theory: three-dimensional curved beam elements, *Computer methods in applied mechanics and engineering* 122 (1-2) (1995) 11–26.
- 1088 [24] P. G. Ciarlet, G. Geymonat, Sur les lois de comportement en   lasticit   non lin  aire compressible, *CR Acad. Sci. Paris S  r. II* 295 (1982) 423–426.
- 1092 [25] M. Destrade, G. Saccomandi, I. Sgura, Methodical fitting for mathematical models of rubber-like materials, *Proceedings of the Royal Society A: Mathematical, Physical and Engineering Sciences* 473 (2198) (2017) 20160811.
- 1094 [26] A. M. Tarantino, Homogeneous equilibrium configurations of a hyperelastic compressible cube under equitriaxial dead-load tractions, *Journal of Elasticity* 92 (2008) 227–254.
- 1096
- 1098

- 1100 [27] A. M. Tarantino, Equilibrium paths of a hyperelastic body under progres-
sive damage, *Journal of Elasticity* 114 (2) (2014) 225–250.
- 1102 [28] L. Lanzoni, A. M. Tarantino, Equilibrium configurations and stability of a
damaged body under uniaxial tractions, *Zeitschrift für angewandte Math-*
1104 *ematik und Physik* 66 (1) (2015) 171–190.
- [29] L. Lanzoni, A. M. Tarantino, A simple nonlinear model to simulate the lo-
1106 calized necking and neck propagation, *International Journal of Non-Linear*
Mechanics 84 (2016) 94–104.
- 1108 [30] F. Falope, L. Lanzoni, A. Tarantino, Bending device and anticlastic sur-
face measurement of solids under large deformations and displacements,
1110 *Mechanics Research Communications* 97 (2019) 52–56.
- [31] L. Lanzoni, A. M. Tarantino, Damaged hyperelastic membranes, *Interna-*
1112 *tional Journal of Non-Linear Mechanics* 60 (2014) 9–22.
- [32] A. M. Tarantino, L. Lanzoni, F. O. Falope, *The bending theory of fully*
1114 *nonlinear beams*, Springer, 2019.